1995ApJ...451..252W

The Astrophysical Journal, 451:252–274, 1995 September 20

THE DENSITY STRUCTURE IN THE ROSETTE MOLECULAR CLOUD: SIGNPOSTS OF EVOLUTION

Jonathan P. Williams
Radio Astronomy Laboratory, University of California, Berkeley, CA 94720
Leo Blitz
Astronomy Department, University of Maryland, College Park, MD 20742
and
Anthony A. Stark
Center for Astrophysics, 60 Garden Street, Cambridge, MA 02138
Received 1994 November 28; accepted 1995 March 10

ABSTRACT

We have analyzed the clumpy structure of the moderately dense, $n_{H_2} \simeq 10^3$ cm^{-3} gas traced by the $J = 1$–0 lines of CO and ^{13}CO in the Rosette Molecular Cloud using Clumpfind, our automatic clump finding algorithm. About half of the clumps are gravitationally bound; about 15% are virialized. The clumps that are not gravitationally bound appear to be bound by the pressure of the interclump medium, which is largely atomic. The clumps in which star formation is known to be taking place tend to be the most massive clumps in the complex and are all virialized or very close to it. Column density profiles of the star-forming clumps are steeper than for the pressure-bound clumps, and are reasonably well described by a form $\rho(r) \propto r^{-2}$. The clump mass spectrum follows a power law, $dN/dM \propto M^{-1.27}$, similar to other giant molecular clouds (GMCs). We argue that the mass spectrum of the clumps does not evolve into the stellar IMF, which originates instead within the individual clumps. The internal density of the clumps measured by ^{13}CO is found to be nearly independent of clump mass. The volume filling fraction of the clumps relative to the entire GMC is 8%; the mean density contrast between the clump and interclump gas is about 40. Column densities are determined using the LTE method, but we find that to achieve consistency between the mass determined from ^{13}CO and the commonly used method using CO alone requires either that $X = N_{H_2}/W_{CO} = 1.1 \times 10^{20}$ cm^{-2} (K km s^{-1})$^{-1}$, or that $N_{H_2} = 1.0 \times 10^6 N_{^{13}CO}$. We favor the former alternative because the cloud does not appear virialized and because the resulting mass agrees better with the dynamical mass of the cloud. We show that the mass of the cloud can be determined well from the ^{13}CO alone and that $N_{^{13}CO}/W_{^{13}CO} = 1.5 \times 10^{15}$ cm^{-2} (K km s^{-1})$^{-1}$.

The clumps exhibit a gradient in velocity of 0.08 km s^{-1} pc^{-1} over the face of the cloud complex. If interpreted as rotation, then the rotational energy is a small fraction of the clump kinetic energy, $6\%/\sin^2 i$, where i is the inclination of the rotational axis to our line of sight. The clump-to-clump velocity dispersion decreases with clump mass, $\sigma_v(c - c) \propto M^{-0.15}$, indicating that the clump ensemble is dynamically evolved, but the system is far from equipartition and most of the kinetic energy of the cloud resides in the random motions of the largest clumps, $T \propto M^{0.4}$. An additional sign of the evolutionary state of the cloud is that the most massive clumps lie closest to the midplane of the complex. It is shown that clumps that are closer to the Rosette Nebula show greater levels of star formation activity than similar clumps further away. There are also gradients in clump excitation temperatures and mean densities with distance to the H II region. We discuss the implications of these observations for the formation of the molecular cloud from an atomic cloud, the evolution of the clump mass spectrum, and the formation of stars.

Subject headings: H II regions — ISM: clouds — ISM: individual (Rosette Nebula) — ISM: kinematics and dynamics — ISM: molecules — stars: formation

1. INTRODUCTION

Molecular clouds are highly inhomogeneous. This is immediately apparent from their observable millimeter wavelength molecular rotational lines: for instance, the critical density of CO is about 10^3 cm^{-3}, an order of magnitude greater than the density of the cloud averaged over its entire volume. The molecules must therefore be clumped into local density enhancements that occupy only a small fraction of the volume of the cloud (i.e., Blitz & Shu 1980; Stutzki & Güsten 1990). Spectral line observations provide both spatial and velocity information on the brightness temperature of the cloud, resulting in a three-dimensional array, $T_b(l, b, v)$. The extra dimension afforded by the velocity axis makes the density structure in the cloud more easily discernible, in addition to important dynamical information. Mapping in molecular tracers such as CS, HCO$^+$, HCN, etc., with high critical densities reveals the dense cores in a cloud and thereby locates the likely regions of star formation (Lada, Bally, & Stark 1991). The total mass at these densities, however, is only a small fraction of the total mass of the cloud (Helfer & Blitz 1995). Observations of lower density tracers, notably CO and its isotopes, provide information on the energetics and dynamics of the bulk of the cloud molecular material and therefore address questions of cloud formation and evolution toward star formation.

In this paper, we analyze CO, ^{13}CO (Blitz & Stark 1986), and H I observations (Kuchar & Bania 1993) of the Rosette Molecular Cloud (RMC, Fig. 1). In future work, we will make similar studies of several other clouds with different star-forming histories in order to compare the arrangement of molecular gas in different environments. We have chosen the RMC as the baseline for such a comparison because it is a prototypical molecular cloud with signs of abundant star formation in its past continuing on to the present day (Cox, Deharveng, & Leene 1991). There are several additional considerations that influenced our choice: the RMC has been well studied (Blitz & Thaddeus 1980) and is the subject of many ongoing investigations (e.g., Block, Dyson, & Madsen 1992; Patel, Xie, & Goldsmith 1993); its location in the outer Galaxy reduces the chances of confusion along the line of sight; and the Rosette Nebula, a large H II region containing 17 OB stars, is favorably located at one end of the cloud, perpendicular to our line of sight, allowing us to observe the effects it may have on the cloud.

We show in § 3 that ^{13}CO is nearly always optically thin in the region of interest, and that nearly all of the emission can be interpreted as coming from discrete clumps that are well separated when viewed in the full three dimensions of the cube. Our analysis of the density structure is, therefore, based predominantly on the ^{13}CO observations. These clumps may be considered the basic building blocks of the cloud, and our analysis proceeds with their identification and categorization (§ 3). The identification of the clumps is accomplished with the automated procedure we have developed and tested on simulated data cubes (Williams, de Geus, & Blitz 1994, hereafter WGB). The algorithm ensures uniformity both within any one cloud, and from cloud to cloud, which is essential when comparing the results of one cloud to another.

Once the clumps have been identified, their properties, e.g., mass, size, and line width are measured and tabulated. In order to determine masses, it is necessary to convert the ^{13}CO column density, $N_{^{13}\mathrm{CO}}$, to H$_2$ column density, N_{H_2}. We determine conversion factors from our data, by insisting that three different methods of calculating the mass give consistent results. These form the basis of the cloud and clump mass determinations that are considered in § 4.1.

Our primary aim is to determine how signatures of cloud formation and evolution are reflected in the clump catalog. To that end, we concentrate first on properties of the clump ensemble: distribution of clump masses, bulk motion of the cloud and dispersion about this motion, and clustering of massive clumps within the cloud (§ 4.2). Second, we examine the relationship between the molecular gas and star formation within the cloud. The association of color-selected *IRAS* point sources with clump positions indicates that star formation is taking place within them: we compare clump properties of star-forming and non–star-forming clumps in § 4.3. The Rosette Nebula has destroyed the southwestern edge of the cloud; in § 4.4 we test for its influence on the remainder of the cloud by examining how clump properties vary with distance from the H II region. Because the clump finding algorithm makes no assumptions about the geometry of the clumps it finds, and because all the clumps are spatially resolved, we have been able to determine the radial column density profile for each clump in our catalog (§ 4.5). Finally, we discuss in § 4.6 the relation between the distribution of molecular gas with that of the neutral atomic hydrogen. Together, the H I and CO observations present a more complete view of the cloud, showing not only the density enhancements but the *interclump gas* between them. We use the results of § 4 to draw some conclusions about the evolution of the RMC in § 5. The major findings of this work are summarized in § 6.

TABLE 1

PROPERTIES OF THE RMC

Parameter	Value
Distance (pc)	1600
Mean LSR velocity (km s^{-1})	13.9
Projected area (pc^2)	2200
CO line width (km s^{-1})	8.1
Mass^a ($M_\odot$)	$1.6 \times 10^5 \mathcal{R}_{\mathrm{RMC}}$
Mean H$_2$ column density^a (cm^{-2})	$4.0 \times 10^{21} \mathcal{R}_{\mathrm{RMC}}$
Mean H$_2$ number density^a (cm^{-3})	$31 \mathcal{R}_{\mathrm{RMC}}$

[a] $\mathcal{R}_{\mathrm{RMC}} = X_{\mathrm{RMC}}/X_{\mathrm{gal}} = 0.48$; see § 4.1.

2. OBSERVATIONS

A number of cloud properties are summarized in Table 1. Mapping of the RMC in the $J = 1\text{–}0$ lines of CO and ^{13}CO was carried out at the 7 m telescope at AT&T Bell Laboratories between 1982 and 1985 and is described in detail in Blitz & Stark (1986). The cloud was almost entirely mapped in CO, but only the main section of the cloud to the west of the H II region was mapped in ^{13}CO. 7637 spectra were obtained in CO and 2213 in ^{13}CO. The extent of the ^{13}CO mapping relative to the CO observations is shown in Figure 1. Data were sampled every 1ʹ.5; the beamwidth is 1ʹ.7, corresponding to 0.7 pc at the 1600 pc distance of the RMC. The velocity resolution and rms noise per channel are, respectively, 0.65 km s^{-1} and 0.7 K for CO, and 0.68 km s^{-1} and 0.25 K for ^{13}CO.

The H I observations were made during 1988 using the 305 m telescope in Arecibo, Puerto Rico, by Kuchar & Bania (1993). Details of the data collection and reduction are contained in that work. A total of 1980 spectra were taken over ~8 square degrees, sampled at 4ʹ, the HPBW of the telescope. This corresponds to 1.9 pc at the distance of the RMC. The velocity resolution is 0.52 km s^{-1}, and typical rms noise temperatures are 0.4 K per channel.

3. CLUMP DECOMPOSITION

The first step in the analysis is the characterization of the density structure. The appearance of the cloud depends very much on which spectral line is used to observe it. Figure 2 is a longitude-velocity map of the H I, CO and ^{13}CO data cubes at the same latitude and the same scale. We see immediately that the contrast is greatest for the ^{13}CO map, and that nearly all of the emission appears to be coming from discrete features that are reasonably well separated in position and velocity; it is these discrete features that we wish to catalog as "clumps." The separation between clumps becomes even more evident when adjacent latitude slices are examined. The CO emission shows less contrast than the ^{13}CO (note that the signal-to-noise ratio in each map is the same), which may be due in part to the larger optical depth of the CO, and partly because a larger fraction of the CO emission may be in a diffuse, non-clumped component. The CO probes lower H$_2$ column densities than does ^{13}CO; it is, therefore, a more sensitive tracer of low-density diffuse molecular emission. The H I shows the least contrast, far less than is accounted for by the larger beam (4ʹ.0 vs. 1ʹ.7), and is distributed differently from the CO and ^{13}CO (we discuss this difference more fully in § 4.6). A few points in

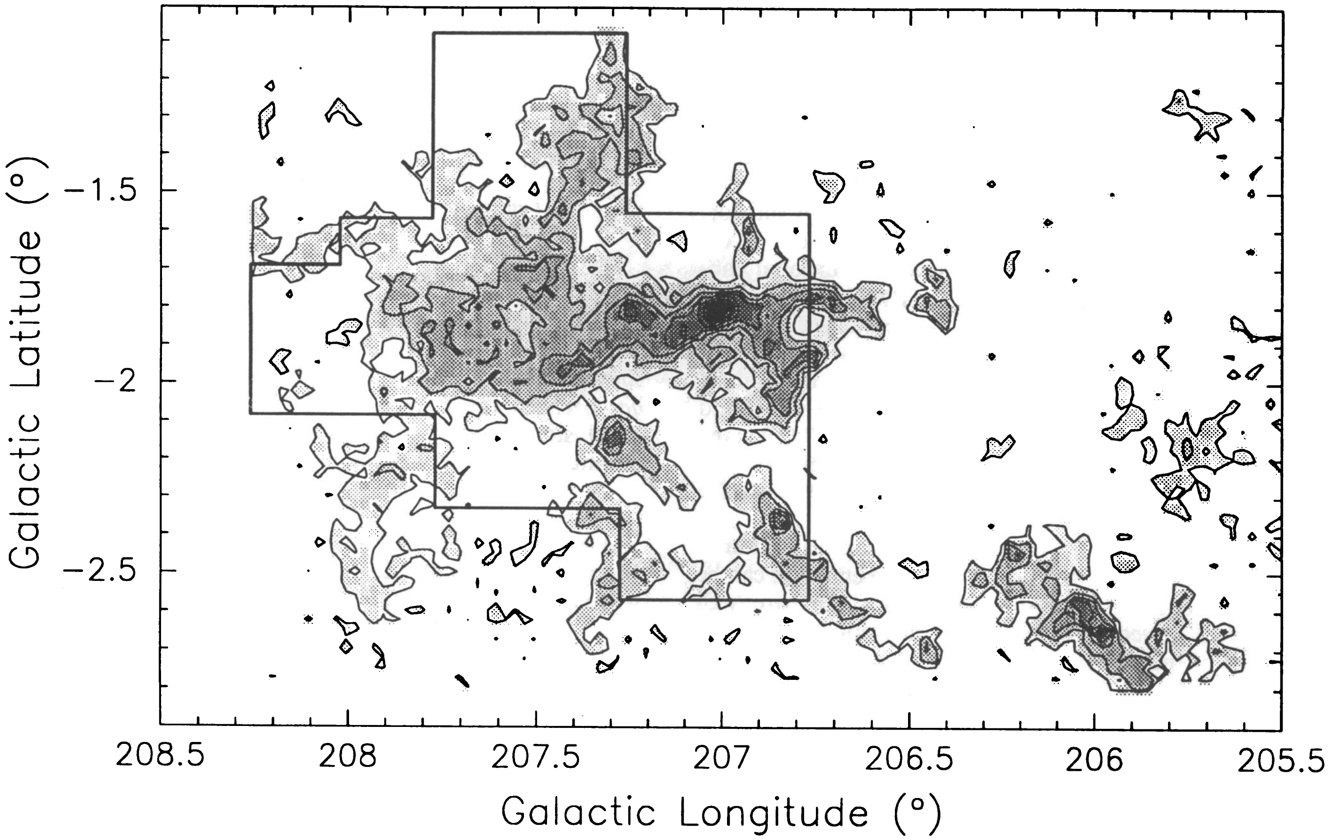

FIG. 1.—Map of the velocity integrated CO emission in the RMC. Spectra have been integrated from $v = 5$ km s^{-1} to 20 km s^{-1}, and the integrated emission plotted as a function of Galactic longitude and latitude. Contours and halftone run from 15 to 120 K km s^{-1} in steps of 15 K km s^{-1}. The region of the RMC that was mapped in ^{13}CO is outlined.

the cloud were observed in C^{18}O at the NRAO 12 m telescope on Kitt Peak (T. Helfer 1995, private communication), and the observed ratio $I_{^{13}\rm CO}/I_{\rm C^{18}O}$ is close to the relative abundances of each species, indicating that the ^{13}CO emission is optically thin. The observed ratio of $I_{\rm CO}/I_{^{13}\rm CO}$ is much less than the relative abundance ratio of each species, suggesting that the CO is optically thick and further that although both species trace the distribution of H$_2$, the CO map is primarily a temperature measure, and the ^{13}CO map is primarily a column density measure.

The CO and ^{13}CO data cubes were analyzed by the WGB Clumpfind algorithm; the CO is used primarily to obtain excitation temperatures for the analysis of the ^{13}CO data cube. We briefly describe the method here. First, the data are contoured in the two position and one velocity dimension at twice the rms noise level of the map, $T_{\rm rms}$, and local maxima in the data cube corresponding to clump peaks are located. The total number of clumps that are found is equal to the number of local maxima. By working down through contour levels, each clump is extended to lower levels of emission, ultimately down to $T = 2T_{\rm rms}$, the lowest contour level. Blending of emission, particularly prominent at the lower contour levels, is handled by splitting up the blended contours in a simple, but justifiable way (see Appendix B of WGB). Clumps that lie on or near the edges of the mapped region are rejected from the analysis.

Once clumps of emission have been isolated in this manner, temperatures, sizes, line widths, and masses are calculated. We follow much the same procedure as in Appendix A of WGB, but in calculating masses we use the CO data to determine the excitation temperature within each clump,

$$T_{\rm ex} = 5.53\left[\ln\left(1 + \frac{5.53}{\langle T_{\rm R}({\rm CO})\rangle + 0.819}\right)\right]^{-1} {\rm K}\,.$$

The quantity $\langle T_{\rm R}({\rm CO})\rangle$ is a weighted average of the CO temperature at the (^{13}CO) clump peak. $T_{\rm ex}$ is, therefore, calculated independently for each clump and is assumed uniform within each one. The ^{13}CO optical depth may then be calculated along each line of sight and integrated to determine the ^{13}CO column density following a procedure originally outlined by Dickman (1978). To convert to molecular hydrogen column densities, and finally to clump masses, we assume $N_{\rm H_2}/N_{^{13}\rm CO} = 5 \times 10^5$, and a helium correction = 1.36.

Castets et al. (1990) and Gierens, Stutzki, & Winnewisser (1992) caution that $\langle T_{\rm R}({\rm CO})\rangle$ may overestimate the excitation temperature of ^{13}CO in regions of large external heating and high column densities, $N_{\rm H_2} > 10^{22}$ cm^{-2}. Thus, the assumption of optical thinness may not be valid for all lines of sight. However, as can be seen from Figure 6 below, the fraction of the RMC that is the subject to the sort of deviations discussed by these authors is small and the correction to the beam-averaged column densities in most cases should also be small and will not change the overall results presented here.

A list of the clump properties derived from the combination of the CO and ^{13}CO observations is in Table 2. The gravitational mass, $M_{\rm grav}$, is defined by the condition $T = |V|$, where T is the kinetic energy, and V is the gravitational potential energy of the clump. In § 4.5, clumps are shown to have density

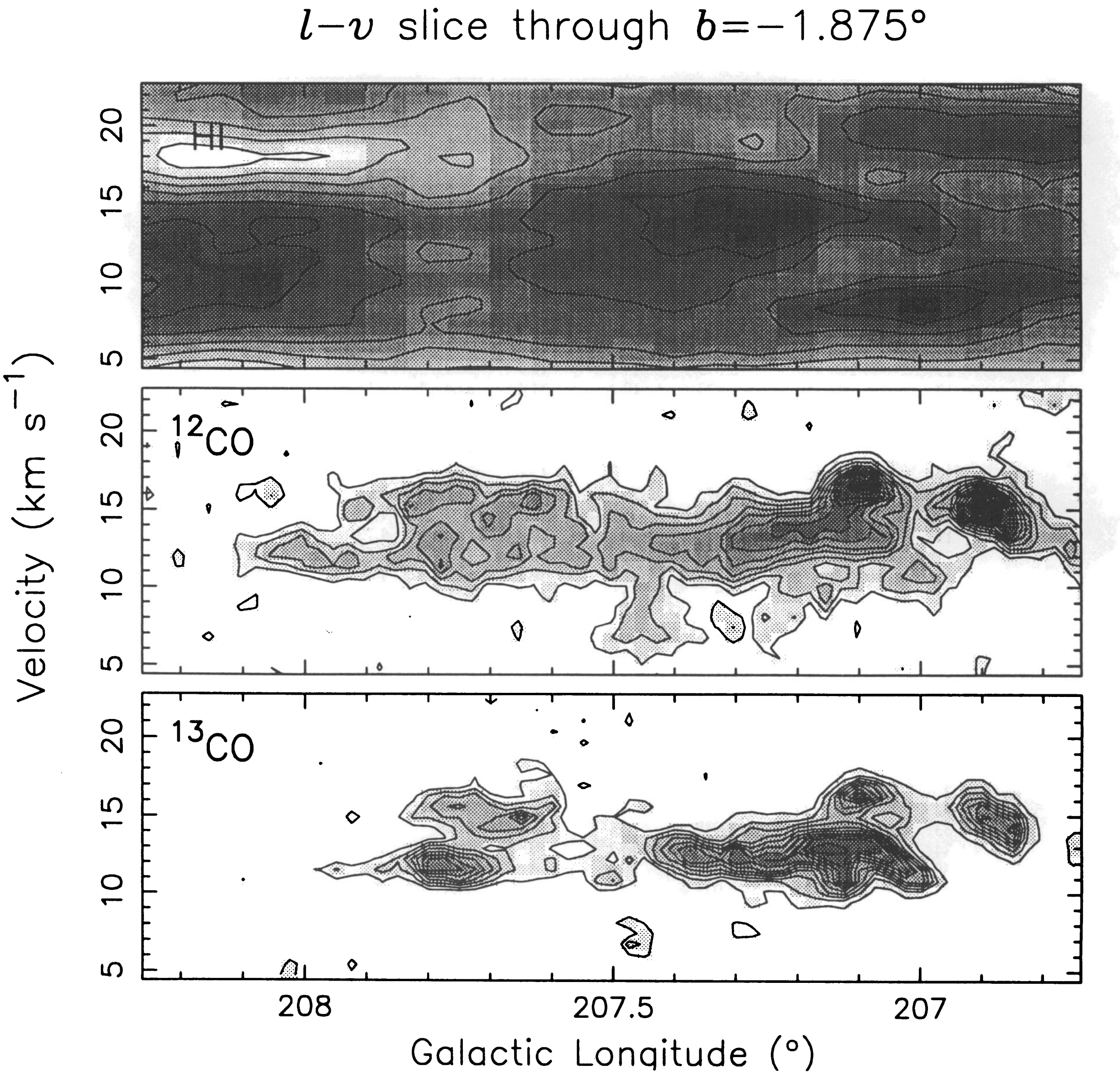

FIG. 2.—Longitude-velocity map at $b = -1\overset{\circ}{.}875$ of H I, CO, and ^{13}CO in the RMC. For the H I, the minimum contour and halftone level is 20 K, and the maximum is 40 K, with contour increments of 2.5 K. Corresponding numbers for the CO are 1.5, 20, 1.5, and for the ^{13}CO they are 0.5, 7.5, 0.5. The signal-to-noise level in the CO and ^{13}CO maps are similar, and the contrast difference that is seen is, therefore, not an artifact of the way the map is presented, but rather a reflection of the difference in optical depth of the two lines, and possibly a diffuse molecular component best seen in CO. The H I is contoured so as to only show the peaks of emission, which appear to anticorrelate with the molecular emission.

profiles that are approximately inverse square. Appendix A of WGB shows that in this case, $M_{\rm grav} = 3R\sigma_v^2/2G$, where R is the clump radius, σ_v is the measured one-dimensional clump velocity dispersion, and G is the gravitational constant ($=1/232$ in units of $M_\odot$, km s^{-1}, pc). The kinetic energy of clumps with masses, $M \simeq M_{\rm grav}$, is in balance with their gravitational energy, and we hereafter refer to these clumps as being gravitationally bound. Clumps with $M \ll M_{\rm grav}$ have motions that are not bound by their gravity, but rather by the surface pressure of the interclump medium (see § 4.6.2). Bertoldi & McKee (1992) have also considered the magnetic energy of a clump, which has the effect of increasing the mass needed for gravitational boundedness. Our definition, $M = M_{\rm grav}$, is equivalent to their $\alpha/a = 2$ (where $a = 5/3$ for an inverse square clump density profile), but we do not include the effects of clump magnetic fields in this work.

Contour maps of seven of the clumps defined by the Clumpfind algorithm are in Figure 3. The clumps have a variety of shapes, but are (with the exception of clump 5) quite centrally condensed (see § 4.6). Associated *IRAS* sources with colors typical of embedded star-forming regions are indicated by the asterisks (∗) and are, again with the exception of clump 5, very close to the peak column density through each clump. The properties of these "star-forming" clumps relative to the others in the cloud are discussed in § 4.3.

4. RESULTS AND DISCUSSION

4.1. *Clump and Cloud Mass Determinations*

Although the CO line is optically thick on the scale of an entire GMC, the integrated CO emission, $W_{\rm CO}$, is observed to be linearly related to the molecular hydrogen column density,

TABLE 2

CLUMPS IN THE ROSETTE MOLECULAR CLOUD

Clump	l_{peak}	b_{peak}	v_{peak} (km s^{-1})	T_{ex} (K)	ΔR (pc)	Δv (km s^{-1})	M_{LTE} ($M_{\odot}$)	M_{grav} ($M_{\odot}$)
1......	207°000	−1°823	15.6	30.9	2.36	2.13	2532	674
2......	207.250	−1.823	12.9	8.3	3.06	2.46	2417	1160
3......	207.550	−1.723	12.9	11.7	4.21	2.44	2373	1572
4......	207.775	−1.773	11.5	8.3	3.77	1.74	2035	723
5......	207.700	−1.923	14.9	9.4	3.60	2.11	1700	1011
6......	207.100	−1.848	10.8	9.9	2.82	1.93	1540	661
7......	207.275	−2.148	15.6	20.3	2.79	1.59	1175	444
8......	207.125	−1.898	12.9	11.3	1.90	1.86	1059	412
9......	207.350	−1.898	12.2	10.4	2.96	2.04	955	780
10......	206.825	−1.998	16.3	19.8	1.94	2.21	934	598
11......	206.850	−2.373	14.2	16.8	2.21	2.08	847	602
12......	207.350	−1.423	12.2	11.4	2.64	2.11	727	738
13......	206.875	−1.898	14.9	19.6	1.99	2.40	701	721
14......	207.075	−1.873	12.9	10.5	1.98	2.18	657	595
15......	207.500	−2.048	10.2	9.3	3.01	2.68	652	1364
16......	207.400	−1.948	16.3	15.8	2.31	1.64	526	390
17......	207.100	−1.873	16.3	17.4	1.95	1.71	467	359
18......	206.775	−1.948	15.6	18.5	1.33	1.74	452	252
19......	207.150	−1.798	12.2	10.3	1.50	1.73	407	282
20......	207.225	−1.573	11.5	8.6	2.23	2.62	372	967
21......	207.675	−1.923	11.5	9.1	2.09	1.41	337	263
22......	206.775	−1.773	12.9	17.3	1.40	2.25	333	444
23......	207.650	−1.573	14.9	10.5	1.89	1.67	298	333
24......	207.900	−1.798	10.8	9.0	1.93	1.46	294	260
25......	207.600	−1.948	11.5	9.1	1.85	1.80	290	378
26......	207.800	−1.773	14.9	9.4	2.17	1.53	221	318
27......	207.850	−1.598	10.8	7.0	2.25	2.70	211	1034
28......	207.600	−1.898	15.6	9.3	1.52	2.08	173	414
29......	206.800	2.523	13.6	8.9	1.42	1.30	164	151
30......	206.975	−2.498	11.5	8.9	1.88	1.48	156	260
31......	207.250	−2.523	16.3	12.3	1.24	1.29	152	130
32......	206.925	−1.648	14.9	13.9	1.31	1.79	150	263
33......	207.325	−2.048	8.1	7.0	2.00	1.45	143	264
34......	207.375	−1.273	14.2	8.7	1.54	1.53	117	226
35......	207.900	−2.048	15.6	8.8	1.55	1.35	103	178
36......	206.825	−2.073	14.2	8.6	1.49	2.25	94	478
37......	207.425	−1.373	6.8	8.6	1.71	1.66	94	296
38......	206.950	−2.073	19.0	9.6	1.45	3.28	84	984
39......	206.925	−1.598	14.2	13.9	0.54	1.41	81	68
40......	207.475	−1.723	5.4	8.8	1.08	1.43	72	138
41......	206.775	−2.498	11.5	9.5	1.14	1.35	68	131
42......	207.500	−1.348	12.9	7.7	1.40	1.98	63	346
43......	207.400	−1.548	7.4	5.7	1.43	2.44	62	538
44......	207.300	−1.073	10.2	7.4	1.02	1.82	62	213
45......	207.275	−1.723	10.2	6.7	1.02	1.91	60	236
46......	207.750	−2.198	11.5	8.2	1.09	2.10	58	300
47......	206.900	−2.248	12.9	11.0	1.14	1.57	58	176
48......	207.275	−1.223	10.2	8.5	0.74	1.40	58	92
49......	207.825	−1.698	14.9	7.9	1.34	1.53	56	199
50......	207.100	−1.648	9.5	8.2	0.80	1.41	56	99
51......	207.250	−2.448	17.0	10.5	0.83	1.05	55	58
52......	208.175	−1.973	10.2	7.2	1.57	1.04	53	108
53......	207.500	−1.873	10.8	6.0	0.76	3.02	43	436
54......	207.475	−1.873	6.8	6.5	1.11	1.42	41	140
55......	206.950	−2.298	17.0	12.5	1.11	1.00	41	70
56......	206.925	−2.423	14.2	7.5	0.76	1.40	40	95
57......	207.500	−1.773	5.4	7.9	1.09	1.95	37	261
58......	207.450	−1.273	13.6	8.6	0.71	1.25	34	70
59......	207.075	−2.498	11.5	8.8	0.87	1.23	33	83
60......	207.575	−2.048	15.6	5.3	0.65	0.95	32	37
61......	207.300	−2.098	12.9	5.3	0.78	0.91	28	40
62......	208.100	−1.723	12.9	5.0	0.70	1.25	27	69
63......	207.300	−1.273	8.8	7.1	0.78	2.34	25	269
64......	207.350	−1.673	9.5	7.9	0.76	2.31	25	257
65......	207.300	−1.923	16.3	6.8	0.52	0.93	20	28
66......	207.500	−1.798	17.6	5.0	0.88	1.45	19	117
67......	207.825	−2.073	12.9	8.4	0.50	0.94	19	28
68......	207.675	−2.073	12.9	5.4	0.69	1.28	17	71
69......	207.075	−2.423	14.9	7.0	0.70	0.96	14	41
70......	207.450	−1.523	15.6	7.4	0.56	0.97	13	33

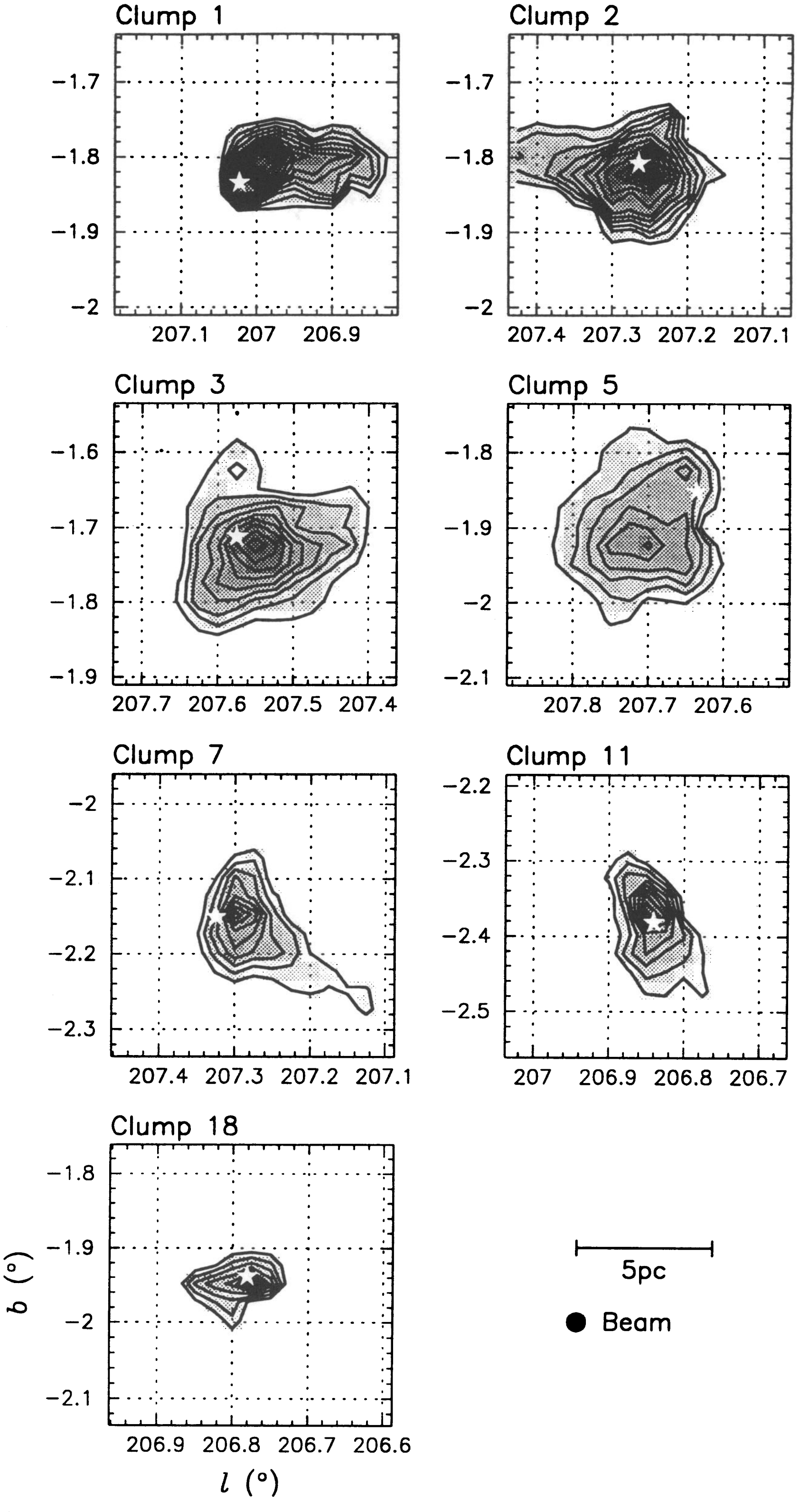

FIG. 3.—Velocity-integrated contour maps of those clumps defined from the Clumpfind algorithm that are associated with an embedded *IRAS* source (see § 4.3). The velocity range of integration varies from clump to clump, chosen to cover all the emission in the clump. Contour levels are at 1.5 × 1.5 cm^{-2} (K km s^{-1})$^{-1}$.

1995ApJ...451..252W

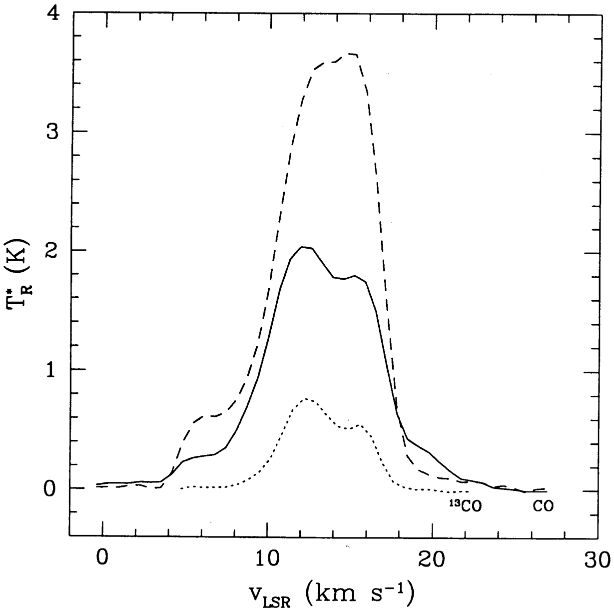

FIG. 4.—Composite spectra of the CO emission in the RMC. The solid line is the average CO spectrum over all lines of sight for which there is detectable emission. The dashed line is the average CO spectrum over all lines of sight for which there is detectable ^{13}CO emission (mapped over a more limited, more intense area), and the dotted line is the average ^{13}CO spectrum over those same lines of sight.

N_{H_2}, through a conversion factor $X = N_{\mathrm{H}_2}/W_{\mathrm{CO}}$ (Bloemen et al. 1986, and references therein). Figure 4 shows that the velocity integrated ^{13}CO emission is less than that of CO by more than a factor of 6, and therefore that it is *generally* optically thin, even though it may be optically thick for a few individual lines of sight. In general, therefore, the ^{13}CO emission directly measures N_{H_2} along each line of sight, and so gives an independent estimate of the mass of the cloud. This section is devoted to checking for consistency between these two mass estimates and, in addition, with the dynamical mass of the cloud. The precise values of the CO/H_2 and ^{13}CO/H_2 conversions are important in determining, for example, the gravitational boundedness of the clumps.

As a first step, we wish to see how the gravitational mass of the cloud compares to the mass determined from W_{CO}, and to the sum of the masses of the clumps that are determined from $N_{^{13}\mathrm{CO}}$. To determine the mass from W_{CO}, we simply multiply the overall integrated CO emission of the cloud by the most commonly used value of X. We wish to compare this mass to the mass determined from the sum of the clump masses but must make a correction to the sum because the ^{13}CO is measured over a smaller area than is the CO. We will then discuss the origin of discrepancies between the two measurements and place an upper limit to the total amount of molecular gas that is not in clumps, but is distributed in a more diffuse component.

4.1.1. *Mass of the Cloud from* CO

Figure 4 shows average spectra of CO and ^{13}CO over two different regions. The solid line is the composite spectrum of CO in the RMC over all lines of sight where it is detected. Here, "detected" means the integrated emission is greater than twice the expected value due to noise, $W_{\mathrm{CO}} > 2(N)^{1/2} T_{\mathrm{rms}}\, \delta v$ where $N = 12$ is the number of channels in the line, δv is the velocity width of a single channel, and T_{rms} is the rms noise per channel; an equivalent equation holds for $W_{^{13}\mathrm{CO}}$. Of the 7637 CO spectra, 4518 show detectable emission, corresponding to an area $A = 2200$ pc^2, and an equivalent circular radius $R = (A/\pi)^{1/2} = 26.5$ pc. The average spectrum integrates to an average $W_{\mathrm{CO}} = 17.6$ K km s^{-1}, which converts to a total (H_2 + He) mass,

$$M_{\mathrm{cloud}} = 1.6 \times 10^5 \mathscr{R}_{\mathrm{RMC}} M_\odot ,$$

where $\mathscr{R}_{\mathrm{RMC}} = X_{\mathrm{RMC}}/X_{\mathrm{gal}}$ is the ratio of the conversion factor for the RMC compared to the most recent value $X_{\mathrm{gal}} = 2.3 \times 10^{20}$ cm^{-2} (K km s^{-1})$^{-1}$ measured for the Galaxy (Dame 1993). Consistency between this mass and the total clump mass derived from the ^{13}CO observations over the same region determines $\mathscr{R}_{\mathrm{RMC}}$.

4.1.2. *Mass of the Cloud from the Sum of the Clump Masses*

The sum of the clump masses in Table 2 is $M_{\mathrm{clumps}} = 2.8 \times 10^4$ $M_\odot$, but these clumps do not account for all the ^{13}CO emission. Three ^{13}CO spectra are presented in Figure 5: an average spectrum for the mapped region, an average spectrum of the clump ensemble, and an average for the mapped region for pixels with $T > 2T_{\mathrm{rms}} = 0.5$ K, corresponding to the lowest contour used in the Clumpfind algorithm. The clumps account for 89% of the emission seen in the third spectrum, showing that the algorithm does assign most of the assignable emission to clumps. There is substantial emission below the first contour level, however, that is not included in the clump mass determinations. Comparison with the average spectrum of all the emission shows that 24% of the clump emission lies below the first contour level, and therefore true clump masses are likely to be, on average, correspondingly higher. On the other hand, some of this emission may be in a diffuse component not assignable to any particular clump. Observations at higher signal-to-noise would allow the first contour level (and the correction for its exclusion) to be lower. When one factors in the correction for the low-level emission near the clump boundaries, the total clump mass comes to $M_{\mathrm{clumps}} = 3.5 \times 10^4\, M_\odot$.

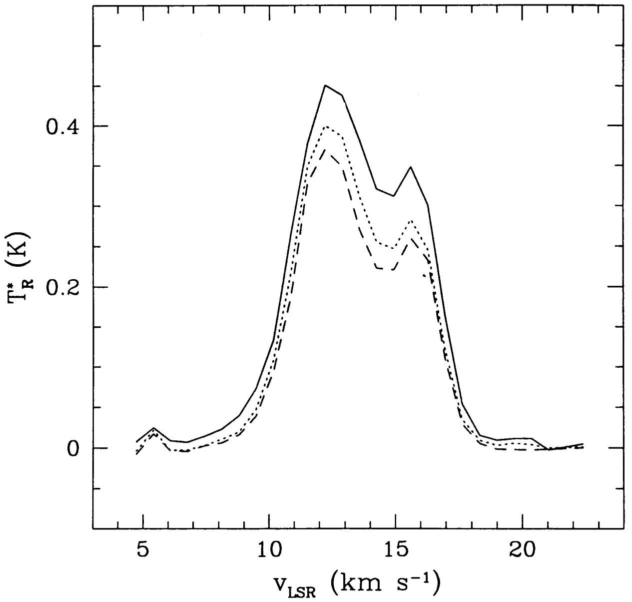

FIG. 5.—Three composite ^{13}CO spectra. The solid line is the average spectrum over all lines of sight, the dashed line is the average spectrum of all the clumps found in the ^{13}CO data cube, and the dotted line is the average spectrum only for pixels with $T > 2T_{\mathrm{rms}} = 0.5$ K (corresponding to the lowest contour level in the Clumpfind routine).

The ^{13}CO observations did not cover the entire cloud, however, but were concentrated toward the regions of brightest emission. This is evident from the average CO spectrum (Fig. 4, *dashed line*) in this region being greater than the average for the whole cloud. The 1311 CO spectra that combine into this average amount to an integrated $W_{\rm CO} = 28.3$ K km s^{-1}. Scaling $M_{\rm clumps}$ by the ratio of $W_{\rm CO}$ inside and outside the areas in which ^{13}CO was observed and by the ratio of the observed areas gives an extrapolated clump mass,

$$M_{\rm clumps} = 7.5 \times 10^4 \ M_\odot \ .$$

This is consistent with the CO mass, $M_{\rm cloud}$, over the same region if $\mathscr{R}_{\rm RMC} = 0.48$, or $X_{\rm RMC} = 1.1 \times 10^{20}$ cm^{-2} (K km s^{-1})$^{-1}$.

4.1.3. *Mass of the Cloud from* ^{13}CO *Measurements Alone*

One may arrive at this result in a different (but equivalent) way independent of any clump decomposition. For the region of detectable ^{13}CO emission (Fig. 4, *dashed and dotted lines*), the ratio $W_{\rm CO}/W_{^{13}\rm CO} = 6.63$. Figure 6 plots the column density of ^{13}CO against the integrated emission $W_{^{13}\rm CO}$ for each line of sight. The deviation from linearity between these two quantities indicates increasing saturation of the line as the column density increases, but significant deviations are important only for a small fraction of the points.

The upper envelope of points in Figure 6 is very well defined and the scatter of points from the fitted line is remarkably small, much smaller than a similar fit using CO measurements. This suggests that ^{13}CO can be used as an effective column density tracer without recourse to other measurements in the moderate density regime. It also suggests that the corrections one needs to make for lines of sight that are optically thick are negligible for the cloud as a whole. If we consider just the slope of the fit, we have $N_{^{13}\rm CO} = 14.7 W_{^{13}\rm CO} = 2.22 W_{\rm CO}$, where the units of $N_{^{13}\rm CO}$ are 10^{14} cm^{-2}, and the units of $W_{\rm CO}$, $W_{^{13}\rm CO}$ are K km s^{-1}. Using the ratio $N_{\rm H_2}/N_{^{13}\rm CO} = 5 \times 10^5$ (the same as for the clumps) to convert to H$_2$ column density then implies

$$X_{\rm RMC} = \frac{N_{\rm H_2}}{W_{\rm CO}} = 1.1 \times 10^{20} \ {\rm K \ km \ s^{-1}} \ ,$$

as before. There is evidence for similar values of X in other clouds: recent γ-ray (EGRET) observations of the Orion and Ophiuchus molecular clouds found values for X of $(1.06 \pm 0.14) \times 10^{20}$ K km s^{-1} (Digel, Hunter, & Mukherjee 1995) and $(1.1 \pm 0.2) \times 10^{20}$ K km s^{-1} (Hunter et al. 1994), respectively.

An alternate prescription for achieving consistency between the CO and ^{13}CO derived masses is to require that the conversion ratio between H$_2$ and ^{13}CO column density be greater than 5×10^5. This value was originally derived by Dickman (1978) on the basis of a linear relation between visual extinction and ^{13}CO column density. Increasing the ratio $N_{\rm H_2}/N_{^{13}\rm CO}$ to 1×10^6 allows $X_{\rm RMC} = X_{\rm gal}$ and sets the mass of the molecular cloud at $1.6 \times 10^5 \ M_\odot$.

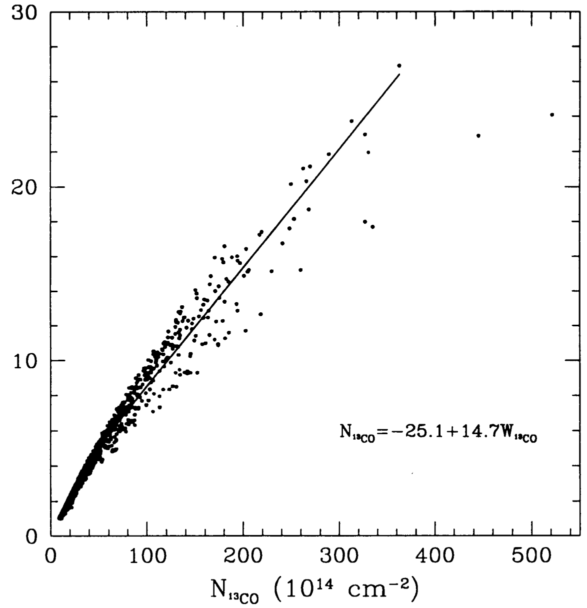

FIG. 6.—^{13}CO column density compared to ^{13}CO integrated line emission for all ^{13}CO spectra in the RMC. The ^{13}CO column density was calculated as described in § 3, using a value for the excitation temperature derived from the peak CO temperature along the same line of sight.

4.1.4. *The Gravitational Mass*

By comparing the CO luminous mass with the gravitational mass of the cloud derived from its size and velocity dispersion, we can independently assess the amount by which $X_{\rm RMC}$ is different from the Galactic value. The (FWHM) cloud line width may be directly measured from the average spectrum of the entire cloud in Figure 4, $\Delta V = 8.1$ km s^{-1}. The equivalent circular radius of the cloud is 26.5 pc, and the gravitational mass (defined in § 3) is

$$M_{\rm grav} = 1.1 \times 10^5 \ M_\odot \ .$$

In practice, it is difficult to determine either the gravitational potential energy or the total kinetic energy of the cloud with precision, and the gravitational mass is probably uncertain by at least 50%. If the RMC is just gravitationally bound, then $M_{\rm cloud} \simeq M_{\rm grav}$, and $\mathscr{R}_{\rm RMC} \simeq 0.7$, again indicating a low CO-to-H$_2$ conversion factor for the RMC relative to the Galactic value.

One might argue that the cloud is virialized in which case $M_{\rm vir} = 2.2 \times 10^5 \ M_\odot$. If this were the case, then $\mathscr{R}_{\rm RMC} \simeq 1.4$ and the conversion from $N_{^{13}\rm CO}$ to H$_2$ would be almost 3 times the value we have adopted. The clump ensemble in the cloud would by assumption be dynamically relaxed and would be in or near energy equipartition. However, we show in § 4.2 that although there is evidence that the cloud shows some dynamical evolution, the cloud is far from being relaxed, suggesting that the lower values for $X_{\rm RMC}$ that we have adopted in this paper are appropriate.

Our derivation of $X_{\rm RMC}$ does not include any correction for atomic hydrogen (or stars) that might be mixed with the molecular gas, in concordance with all other previous work. However, we do make an estimate of the correction to the mass of the cloud from H I measurements in § 4.6 and conclude that it is probably no more than about 30%.

We may parameterize the situation as follows: for consistency between mass estimates from the ^{13}CO and CO emission, we require that

$$\mathscr{R}_{\rm RMC} \equiv \frac{X_{\rm RMC}}{2.3 \times 10^{20} \ {\rm K \ km \ s^{-1}}} = 0.48 \, \frac{N_{\rm H_2}/N_{^{13}\rm CO}}{5 \times 10^5} \ .$$

This conclusion is independent of the distance to the cloud and therefore any errors in its determination. A relatively low value of $X_{\rm RMC}$ is also required for consistency between the luminous mass of the RMC and its gravitational mass, although this constraint is more uncertain because of the unknown geometry and the run of the density (there is additional uncertainty introduced here because the gravitational mass and luminous mass scale differently with distance).

We may summarize this section by concluding that all of the masses are in agreement with a total spread of a factor of 3. We may therefore assume that the mass is determined to an uncertainty of about 75%. In the remainder of this paper we will assume that clump masses (and densities, etc.) derived from ^{13}CO are correct, but that the total cloud mass derived from the CO is smaller by a factor of 2 than the value derived using the Dame (1993) value of $N_{\rm H_2}/W_{\rm CO}$ for the Galaxy.

4.2. *Clump Properties*

The location of the clumps is plotted schematically against the lowest contour of ^{13}CO emission from the RMC in Figure 7. The area of the filled circles is proportional to the mass of the clumps and does not necessarily represent the shape or actual extent of the clumps. There is a range of masses, and the most massive clumps are concentrated toward the midplane of the cloud. Clump velocities across the cloud are displayed in a similar way in Figure 8, which overlays clumps on a projection of the cloud in longitude. There is a velocity gradient: clumps at lower longitude have a greater radial velocity, on the average, than clumps at higher longitudes. As in the *l-b* plot, the most massive clumps are more clustered than less massive clumps. Clearly, even without examining individual clump properties, there is a great deal of information about the cloud contained in the number, spatial, and velocity distributions of the clumps.

4.2.1. *Clump Mass Spectrum*

We discuss first the number distribution with mass, or mass spectrum of the clumps that is plotted in Figure 9. The plot shows that there are more clumps of lower mass than higher mass (down to our sensitivity limit $\sim 30\ M_\odot$) such that the number of clumps in equal logarithmic intervals in mass closely follows a power law, $dN/d\ln M \propto M^{-0.27\pm0.09}$, or equivalently, $dN/dM \propto M^{-1.27}$. We defer discussion of the shaded region of the plot to the following subsection.

The power-law slope is slightly shallower than that measured previously for the RMC as well as for other clouds (see

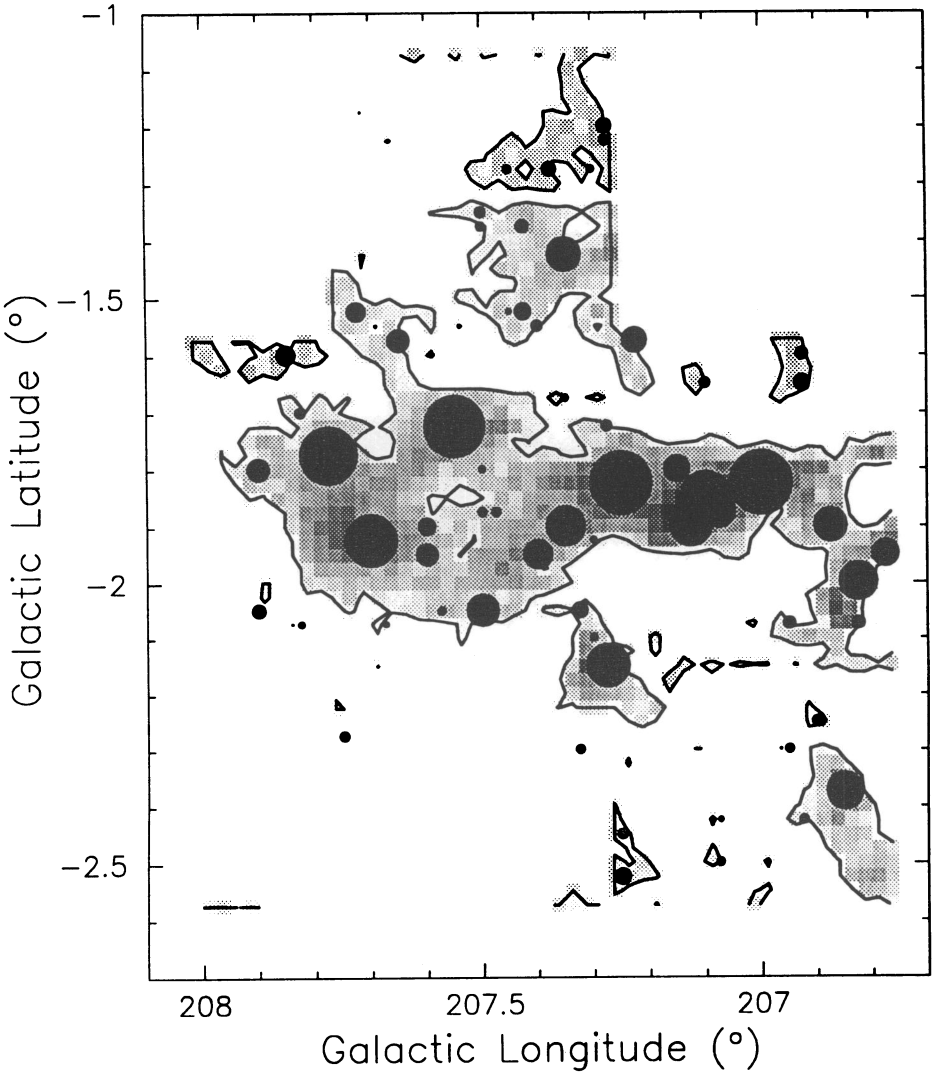

FIG. 7.—Schematic location of the clumps overlaid on a velocity integrated map of the RMC. The contour level is 3 K km s^{-1}. The area of the circle marking each clump's position is proportional to its mass, although the clumps found by Clumpfind are not necessarily spherical.

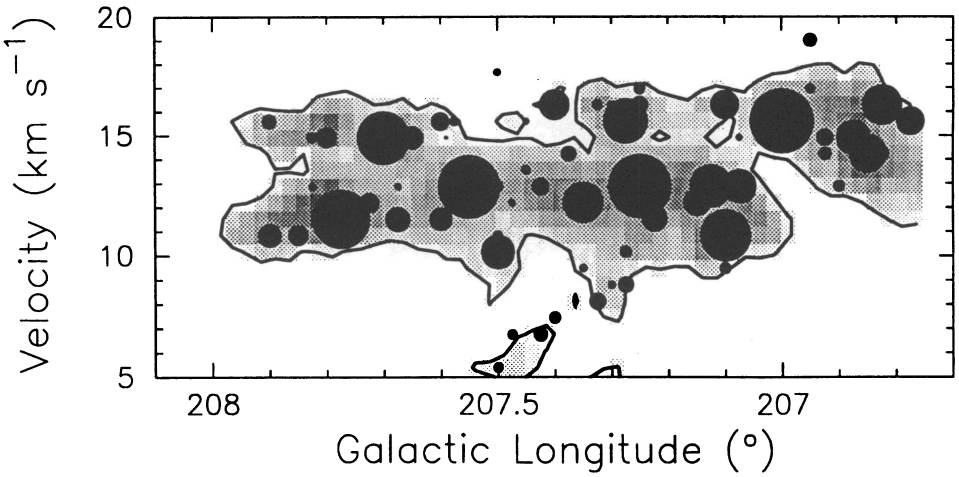

FIG. 8.—Schematic location of the clumps overlaid on a longitude-velocity map of the RMC. The data cube has been integrated over latitude, and a single contour drawn to 20 K′ to show the outline of the cloud. As in Fig. 7, a clump's representation in this figure is not necessarily a true reflection of its shape or extent, and only a measure of its mass.

review by Blitz 1993), and that predicted by collisional agglomeration growth models for clumps (Kwan 1979). Nevertheless, the clumpy structures of all clouds share the characteristic of being dominated in numbers by low-mass clumps, but in integrated mass by a few high-mass clumps. In this fundamental sense, the mass spectrum of clumps is very different from the stellar IMF, $dN_*/dM_* \propto M_*^{-2.25}$ (Scalo 1986), for which both the number *and* total mass of stars is greatest at the lowest masses, implying that further fragmentation occurs before free-fall collapse to protostars.

It is also apparent from Figures 7 and 8 that there is no single dominant clump: there are several clumps of about the same maximum mass, $M \simeq 2\text{–}3 \times 10^3\ M_\odot$, distributed throughout the cloud. This is also reflected by the abrupt cutoff in the mass spectrum, indicating that there may be some physical process limiting the size of the largest clumps in the cloud, analogous to an upper limit to the luminosities of OB associations (McKee & Williams 1995) and the masses of GMCs (Williams & McKee 1995). In this case, the mass may correspond to the magnetic critical mass (Bertoldi & McKee 1992), or clump Jeans mass (§ 4.3), which if exceeded leads to rapid gravitational collapse.

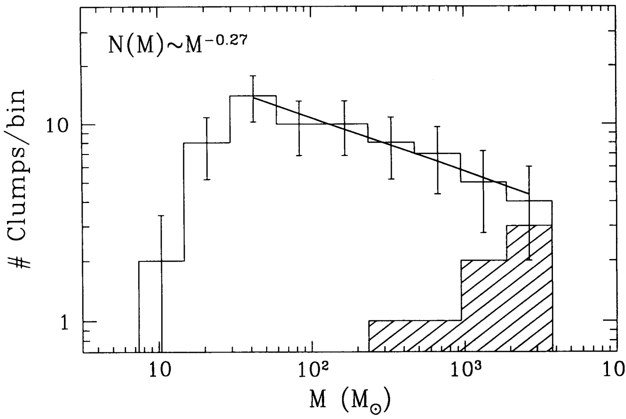

FIG. 9.—Mass spectrum of the clumps in the RMC. Clump masses have been binned at equal logarithmic intervals, $\Delta \log_{10} M = \log_{10} 2$. The ordinate is the number of clumps in each bin, equivalent mathematically to $dN/dM\,\Delta M$. A power-law fit has been made to all but the two lowest mass bins, and is indicated by the solid line on the fit, and by the label at the top left corner. The distribution of clumps with associated *IRAS* sources are indicated by the hatched area.

4.2.2. *Velocity Gradients and Rotation*

We now turn our attention to the spatial and velocity distributions of the clumps. Like many other GMCs (e.g., Blitz 1993), the RMC possesses a systematic velocity gradient, recognizable by the smooth shift in the center of emission along the velocity axis of the data cube (Fig. 10). The clumps can be used to trace this gradient. In what follows we use the Clumpfind routine to find the clumps in CO, and use these results to examine the velocity gradient because more of the cloud was mapped in CO than in ^{13}CO, and the results are more readily apparent using the CO data.

There is a clear correlation between clump central velocity and both longitude and latitude. The gradient, therefore, is not parallel to either axis. We make a three-parameter, linear, least-squares fit to the velocity of a clump as a function of its position, (l, b),

$$v(l, b) = v_0 + \frac{\partial v}{\partial l}(l - l_0) + \frac{\partial v}{\partial b}(b - b_0) .$$

Here, v_0 is a constant mean velocity of the cloud due to the differential rotation of the Galaxy, and (l_0, b_0) is an arbitrary reference position (in this case, the emission weighted mean). If the velocity gradient is interpreted as rotation, then the axis of rotation, defined by $v = v_0 =$ constant is

$$\frac{l - l_0}{b - b_0} = -\frac{\partial v/\partial b}{\partial v/\partial l} ,$$

which is overlaid on a velocity integrated map of the cloud in Figure 10. Clump velocities are plotted as a function of perpendicular distance, s, from this axis in Figure 11. Mass-weighted averages in bins of size $\Delta s = 5$ pc are overlaid, and the linear fit through the individual points is also displayed. The plot actually displays the fit to emission peaks in the CO map because the full extent of the cloud can then be used to define the gradient. The ^{13}CO clump analysis shows a very similar axis and gradient, but the trend is not as clear because of the limited range of the ^{13}CO mapping. The fitted velocity gradient $dv/ds = 0.08$ km s^{-1} pc^{-1}. This value is about half of the value quoted for the cloud by Blitz (1993) from lower

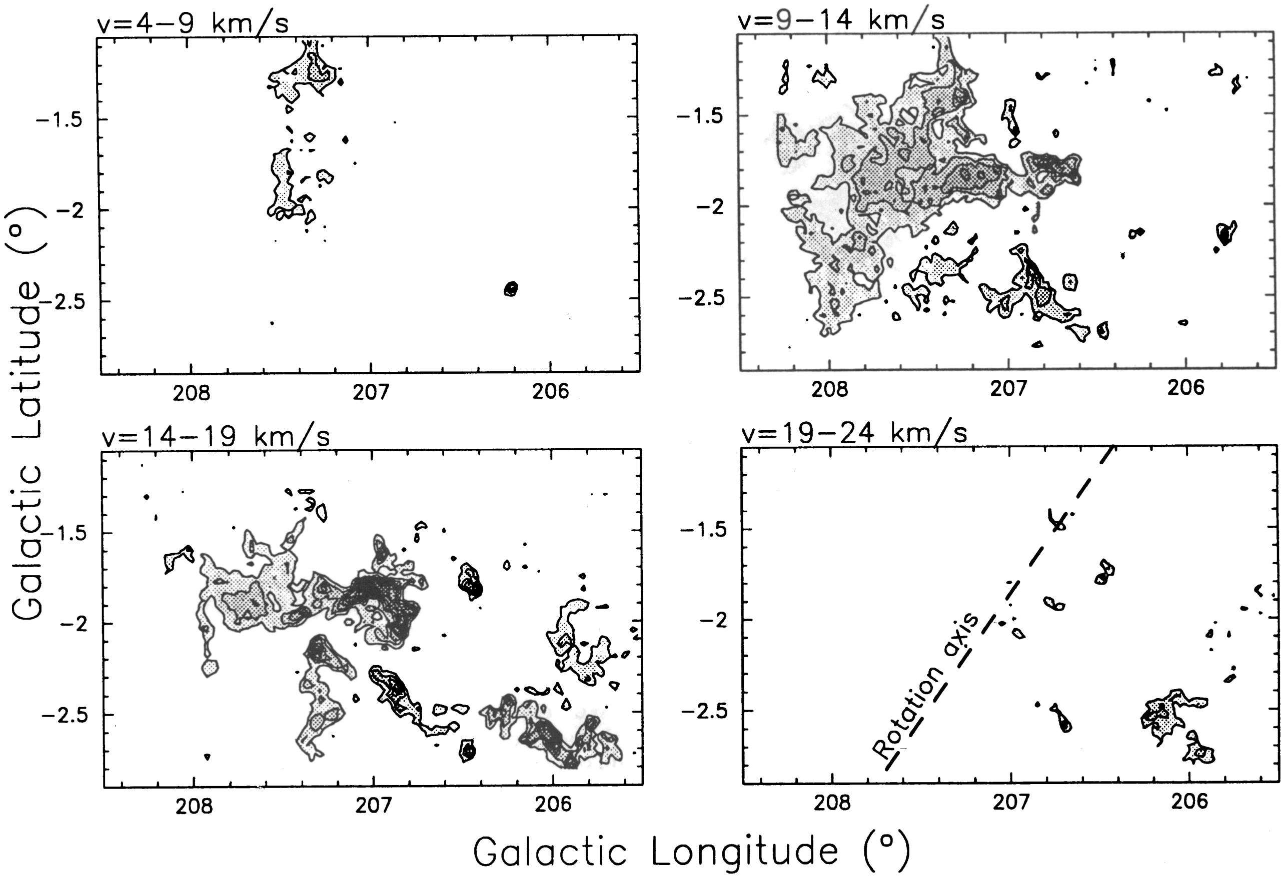

FIG. 10.—Four maps of the RMC integrated over different velocity ranges (*top of each panel*), to show the variation of cloud emission with radial velocity. Contours and halftone range from 5 to 50 K km s^{-1} in steps of 5 K km s^{-1}. The dashed line in the fourth panel indicates the rotation axis that best fits the average (linear) gradient of the cloud. If the gradient is not due to rotation, then this axis (and lines parallel to it) are simply lines of constant velocity.

resolution CO observations but is probably more accurate. The value of 0.08 km s^{-1} pc^{-1} is also a lower limit to the true value of the gradient because of the unknown inclination of the gradient to our line of sight.

Independent of the inclination, the observed FWHM line width of the cloud as a whole, $\Delta v_{\rm tot} = 8.1$ km s^{-1}, results from a combination of the projected gradient, $\Delta v_{\rm grad}$, and a turbulent component, $\Delta v_{\rm turb}$. The gradient extends along the length of the cloud for about 80 pc, and therefore $\Delta v_{\rm grad} \simeq 3.2$ km s^{-1}. Using $\Delta v_{\rm tot}^2 = \Delta v_{\rm grad}^2 + \Delta v_{\rm turb}^2$, we find $\Delta v_{\rm turb} = 7.4$ km s^{-1}, and the kinetic energy of the (isotropic) turbulent motion is

$$T_{\rm turb} = \frac{3}{2} M \left(\frac{\Delta v_{\rm turb}}{2.355}\right)^2 .$$

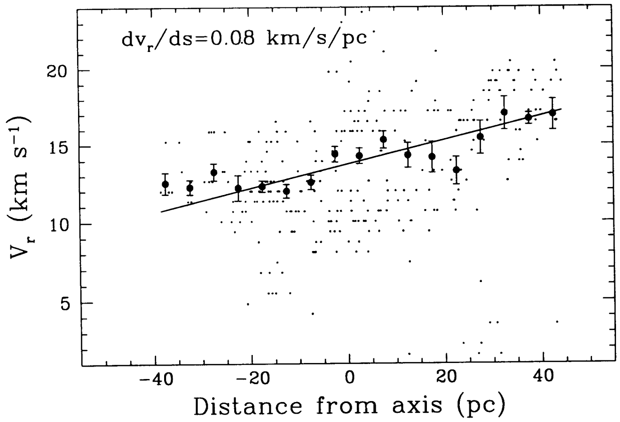

FIG. 11.—Central velocity of clumps as a function of the distance from the axis defined in Fig. 10. A linear fit through all the points is indicated and implies a velocity gradient $dv/ds = 0.08$ km s^{-1} pc^{-1}. Velocities have also been binned every 5 pc to show how the mass-averaged velocities vary systematically across the cloud.

The energy of the ordered motion in the gradient is

$$T_{\rm grad} = \frac{1}{2} M \left(\frac{\Delta v_{\rm grad}}{2.355 \sin i}\right)^2 ,$$

where i is the inclination angle of the gradient to our line of sight (a similar expression would result were the gradient interpreted as rotation). The ratio of these two energies is

$$\frac{T_{\rm grad}}{T_{\rm turb}} = \frac{1}{3 \sin^2 i} \left(\frac{\Delta v_{\rm grad}^2}{\Delta v_{\rm turb}^2}\right) = \frac{0.06}{\sin^2 i} ,$$

and is greater than unity only for $i < 14°$, a rather extreme projection. We conclude that the cloud dynamics are most likely dominated by turbulent motions and not by an overall, systematic motion.

4.2.3. *Clump-to-Clump Velocity Dispersions*

The low value of the above ratio implies that the cloud dynamics are dominated by the unordered, or random, motions of the clumps in the cloud. Figure 12 plots the distribution of this component of the velocity field as a function of clump mass (note that we are once again considering the clumps identified in ^{13}CO). The deviation from the cloud

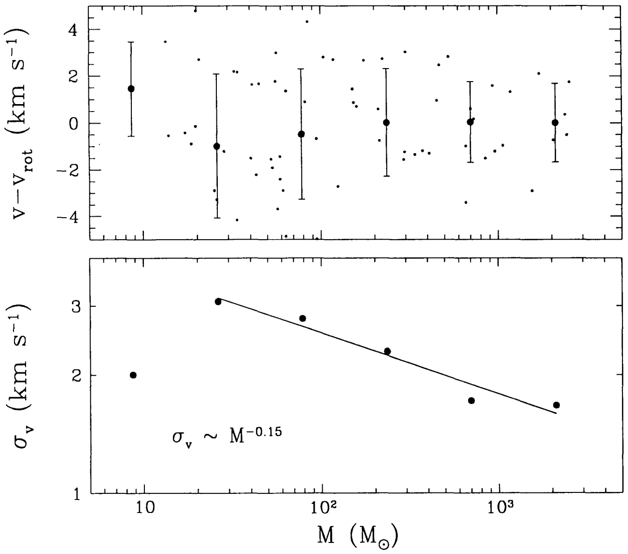

FIG. 12.—Deviation from the mean velocity gradient as a function of mass. The velocity gradient is defined in Fig. 11. The mean deviation and the dispersion about the mean are indicated for equal logarithmic mass bins by the solid circles and error bars. The mean deviation is close to zero, but the dispersion decreases as the clump mass increases. This decrease is plotted in the lower panel, and a power-law fit is applied to all but the lowest mass bin.

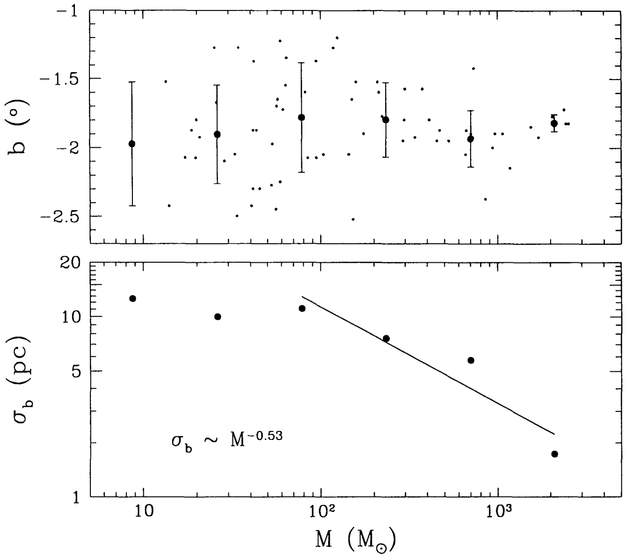

FIG. 13.—Same as Fig. 12, but the dispersion about the mean latitude is plotted for different clump mass ranges. The binning interval is the same as for Fig. 12. There is a steep decrease in the dispersion about the midplane of the cloud for the highest mass clumps indicating a central concentration of the cloud, in turn indicative of dynamical evolution of the clump ensemble.

velocity gradient is plotted for each clump. The mean deviation is close to zero for each mass interval, but the clump–clump dispersion, $\sigma_v(c - c)$, about the mean decreases as the clump mass increases. A power-law fit finds $\sigma_v(c - c) \propto M^{-0.15}$, similar to, but somewhat shallower than that previously found from identifying clumps and clump properties by eye (Blitz 1987, 1990) That the most massive clumps are more tightly clustered about the mean motion of the cloud is an indication that some dynamical evolution of the clump ensemble has taken place. However, the system is not in equipartition: the energy distribution,

$$T_{\rm turb}(M) = N(M)\left(\frac{3}{2}\right)M\sigma_v^2(c - c) \propto M^{0.4} ,$$

is, in the same sense as the integrated clump mass, dominated by the most massive clumps. Additional evidence for dynamical evolution lies in the spatial arrangement of the clumps in the cloud. Figure 7 shows that the most massive clumps are preferentially situated near the midplane of the cloud. We plot in Figure 13 the clump–clump dispersion in latitude, $\sigma_b(c - c)$, against clump mass. The most massive clumps, $M \gtrsim 1000\ M_\odot$, are strongly concentrated at $b \simeq -1\overset{\circ}{.}8$, although the binned average dispersion does not fit a power law as neatly as the velocity dispersion.

4.2.4. *Filling Fraction and Dynamical Evolution*

We showed in § 4.1.2 that 11% of the ^{13}CO emission above the 2 σ contour was not assigned to clumps, and that 24% of the emission is below the 2 σ contour where the algorithm stops. We can, therefore, set a strict upper limit of 35% of the ^{13}CO emission as not being in identifiable clumps, though the percentage is probably much less. That the contrast of the CO emission in Figure 2 is less than that of the ^{13}CO also suggests that some of the molecular gas is not in identifiable clumps, but it is difficult to determine precisely how much. On the other hand, we may estimate the molecular volume filling fraction by taking $\langle N_{\rm H_2}\rangle/\langle n_{\rm clump}\rangle L$, where the angle brackets denote average quantities over the cloud, the densities refer to H_2 densities, and L is the mean depth of the cloud taken as the square root of the projected surface area of the cloud seen in CO. The mass-weighted mean clump density is $\langle n_{\rm clump}\rangle = 220$ cm^{-3} (see § 4.3), the mean column density of H_2 in the same region is $\langle N_{\rm H_2}\rangle = 2.5 \times 10^{21}$ cm^{-2} (Figs. 5 and 6), and $L = 47$ pc (Table 1); thus the filling fraction is 7.8%. This fraction is independent of the ^{13}CO/H_2 conversion factor and is somewhat reduced when atomic hydrogen is included (see § 4.6).

Regardless of the amount of molecular gas not in clumps, the filling fraction is quite low, as has been previously reported (Blitz & Thaddeus 1980), and it seems safe to conclude that the clumps comprise the dominant fraction of the mass of the cloud. The clumps collectively define the gravitational potential that, in turn, defines their motions in the cloud. Such a system is expected to experience significant dynamical evolution in a few crossing times, $t_c \simeq 2R/\Delta V \simeq 80$ pc/8 km s^{-1} $\simeq 10^7$ yr. For $N = 100$ clumps, relaxation of the clump ensemble would occur in $0.1N/\ln N \simeq 2.2$ crossing times (Binney & Tremaine 1987), comparable to the expected lifetime of the cloud (Bash, Green, & Peters 1977; Blitz & Shu 1980; Leisawitz 1990; Williams & McKee 1995). In fact, the situation is likely to be more extreme than the above (collisionless) equations predict: clump collisions are highly inelastic, so it is likely there is agglomeration and rapid dissipation within a crossing time. Using the relations of Blitz & Shu (1980) and the volume filling fraction above, we find that the clump collision time is 8×10^6 yr. It is, therefore, not surprising that the clump ensemble shows dynamical evolution; the clump collision time is less than the age of the older subgroups (Blitz 1987, and references therein), and collisions and collisional agglomeration should have played an important role in the evolution of the Rosette Molecular Cloud.

4.3. *Star Formation in the RMC*

We have searched the *IRAS* Point Source Catalog, Version 2 (1988, hereafter the PSC; *IRAS* Explanatory Supplement 1988) for far-infrared sources that match the color indices of

TABLE 3

IRAS POINT SOURCES ASSOCIATED WITH THE RMC

l	b	FLUX DENSITY (jy) 12 μm	 25 μm	 60 μm	 100 μm	L ($L_\odot$)	CLUMP
$207\overset{\circ}{.}27$	$-1\overset{\circ}{.}81$	78.44	375.20	958.80	995.20	11000	2
207.33	−2.15	13.35	38.29	602.60	949.00	5100	7
206.84	−2.38	8.44	21.45	252.60	498.80	2500	11
207.02	−1.83	6.08	6.48	129.30	323.60	1400	1
206.78	−1.94	3.02	11.96	88.52	247.20	1100	18
205.93	−1.66	1.46	1.89	35.78	130.00	480	
206.87	−1.73	1.07	1.49	27.34	118.30	410	
205.92	−1.69	1.54	2.04	30.33	95.07	380	
205.93	−2.14	0.74	1.01	21.72	102.60	340	
207.64	−1.85	0.72	2.50	27.26	67.01	300	5
207.31	−2.54	1.45	4.42	30.00	43.96	290	
208.63	−2.90	0.58	4.53	25.43	51.45	270	
207.58	−1.71	0.40	0.96	5.00	12.26	60	3
207.39	−1.20	0.25	1.10	4.86	7.38	50	

typical star-forming regions in other molecular clouds (Wouterloot et al. 1990; Wouterloot & Walmsley 1986). We require that there be firm detections in the 25, 60, and 100 μm bands, that the flux at 25 μm be greater than at 12 μm, and that the colors satisfy

$$0 < R_{23} < 1.5 ,$$

$$-1 < R_{34} < 0.261 + 0.227 R_{23} ,$$

where $R_{ij} = \log_{10} (\nu_j S_j / \nu_i S_i)$ and $i = 1, 2, 3, 4$ corresponds to $\lambda = 12, 25, 60$, and 100 μm, respectively.

There are 14 sources that satisfy the above criteria and lie in the range $205\overset{\circ}{.}0 < l < 208\overset{\circ}{.}5$, $-3\overset{\circ}{.}0 < b < -1\overset{\circ}{.}0$. We have listed their positions, the flux in each band, F_ν, and the total luminosity, $L_{\rm IR} \propto \sum \nu F_\nu$, in Table 3 and have also plotted their location, with size a measure of luminosity, on a velocity-integrated CO map in Figure 14. The most luminous source at the approximate center of the cloud is AFGL 961 (Cohen 1973; Castelaz et al. 1985); other sources have also been observed in detail (Hanson et al. 1993). There is a clear correlation between the sources and the molecular gas. Of these sources, seven lie within one FWHM size of a ^{13}CO clump peak indicated in the

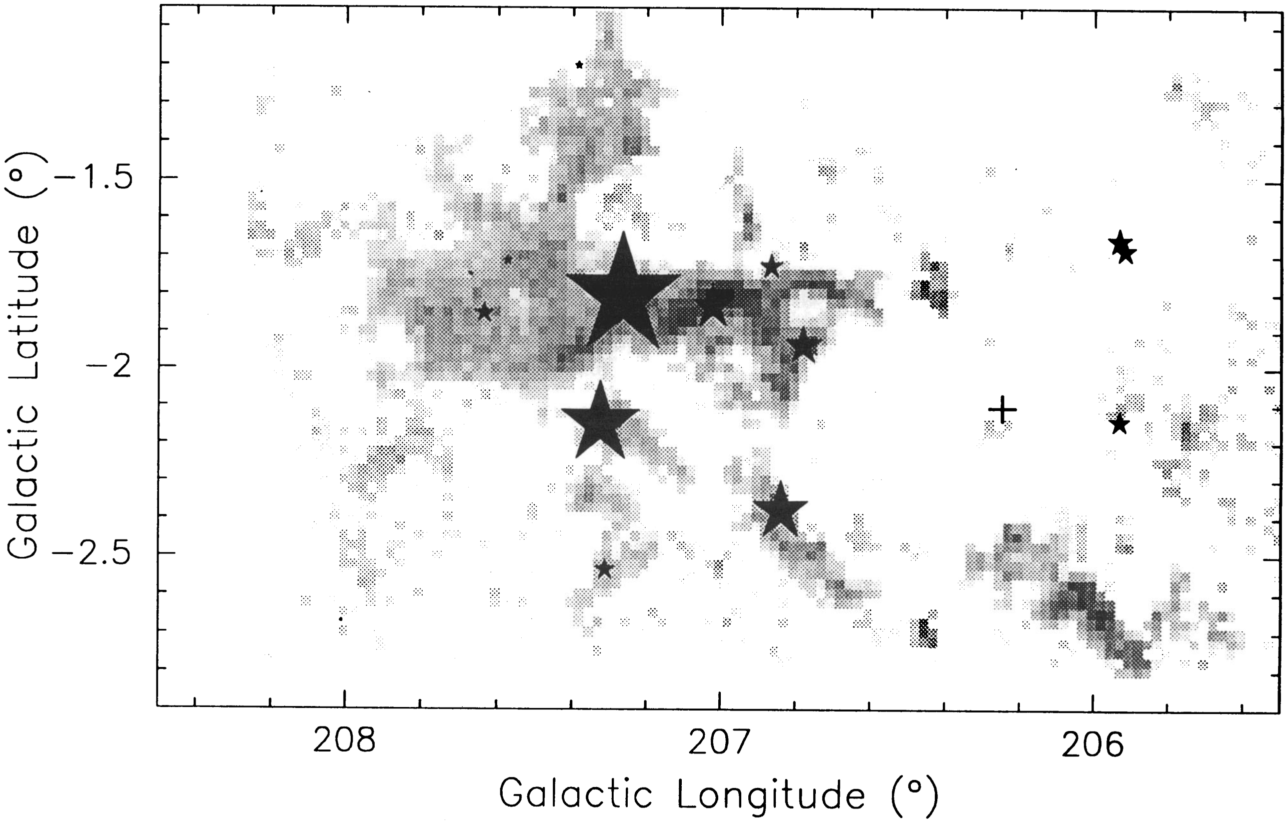

FIG. 14.—Velocity-integrated map of the RMC in halftone ranging from 15 to 120 K km s^{-1}. Stars indicate the positions and luminosities of the *IRAS* point sources associated with the cloud. The area of each symbol is proportional to the infrared luminosity of the source (listed in Table 3).

table and plotted in Figure 3. Hereafter, these clumps are considered "star forming".

Our selection of the *IRAS* sources is similar to the analysis of Cox et al. (1991) who first listed the locations of the infrared star-forming regions in the RMC. They relied on simply having detections in each band above a fixed limit defined for each band rather than the more detailed color criteria that we have employed. Their list also contains sources that are reliably detected, but for which the flux is not reliably measured; sources that we rejected. All the sources in Table 3 are contained in the Cox et al. compilation: our list is a subset of theirs, but may be considered more quantitative in that it is defined by a strict color criterion and by sources with well-measured luminosities. The major regions of embedded star formation in the RMC are contained in this list.

Can we identify any unusual characteristics of the star-forming clumps? We return to the mass spectrum in Figure 9. The shaded part of the distribution corresponds to the star-forming clumps, which are some of the most massive clumps in the RMC, and therefore also possess relatively large sizes, line widths, and excitation temperatures. It might be expected that the star-forming clumps should be denser than their non–star-forming counterparts. We can calculate average clump densities from the clump mass, M, and projected area, A, assuming that the clump volume varies as $A^{1.5}$, or, alternatively, we can divide the peak column density of each clump by its size. Either way, we find that the mass-weighted mean clump density is $n_{\mathrm{H_2}} = 220\ \mathrm{cm^{-3}}$, in good agreement with the results of Bertoldi & McKee (1992). A histogram of average clump densities is plotted in Figure 15: there is little variation in average density from clump to clump, and there are no strong correlations with clump mass, gravitational parameter, α, or star-forming nature of the clump. The lack of variation is likely due to the limited density range over which the observed ^{13}CO line is strongly excited, and does not necessarily reflect the amount of denser gas, $n_{\mathrm{H_2}} \gtrsim 10^4\ \mathrm{cm^{-3}}$, within each clump that can be observed in molecular lines of, e.g., CS, HCN, or HCO$^+$. A very low-sensitivity CS map of the central region of the cloud shows that there is emission associated with the massive ^{13}CO clumps. We ran the Clumpfind program on the data cube to precisely locate the centers of the four most reliable identifications and found that they coincide with clumps 1, 2, 5, and 18; all associated with *IRAS* sources (Table 3). However, we cannot make further conclusions regarding the distribution of dense gas in other clumps because of the low sensitivity of the map.

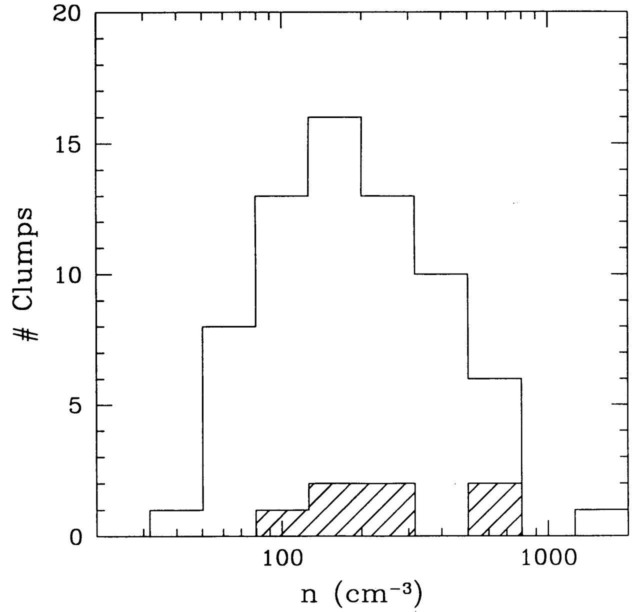

FIG. 15.—Distribution of clump average densities. $n_{\mathrm{H_2}}$ is calculated from the mass and projected area of the clump assuming that clump volume scales with area. Most clumps have densities $n_{\mathrm{H_2}} \simeq 200\ \mathrm{cm^{-3}}$. Star-forming clumps are shaded.

There is a clearer correlation between the star-forming clumps and the ratio of kinetic to gravitational energy in a clump, $M_{\mathrm{grav}}/M = 3R\sigma_v^2/2GM$. Figure 16 shows the variation of this ratio with clump mass. The ratio decreases with M, implying the increasing relative strength of self-gravity for the massive clumps. The dotted line at $M_{\mathrm{grav}}/M = 1$ corresponds to gravitational boundedness ($T = |V|$). The seven star-forming clumps all lie well below this line, and they have some of the most extreme values of the ratio.

Note that a few of the clumps have $M > 2M_{\mathrm{grav}}$, greater than expected even for virialization. This is possible if their masses have been underestimated, which could result if a significant fraction of the ^{13}CO emission in the clump is optically thick, or if the magnetic energy in the clump is comparable to its kinetic energy. In fact, all the clumps that are detected in CS have $M > 2M_{\mathrm{grav}}$, including two of the most extreme cases. In all but one case, the LTE mass is underestimated by no more than a factor of 2 to bring the clump into virial equilibrium. This suggests that the star-forming clumps have differences that are even more extreme than the rest of the clump ensemble.

The ratio $R\sigma_v^2/GM$ is a fundamental parameter of clump dynamics, measuring not only the ratio of clump kinetic energy to gravitational potential, but occurring also in the ratio of turbulent pressure to gravitational pressure, and Jeans mass to clump mass (Bertoldi & McKee 1992). These authors also pointed out that the observed correlation between this ratio

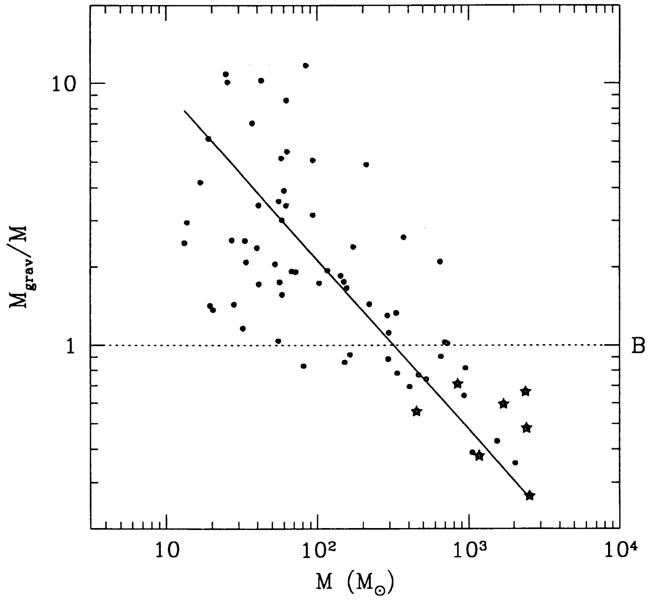

FIG. 16.—Variation of the ratio of clump kinetic energy to gravitational potential with clump mass. The dotted line corresponds to $M = M_{\mathrm{grav}}$ (gravitational boundedness). Star-forming clumps are indicated by the star-shaped symbols, and all lie well below the line. The least-squares fit shows that the ratio decreases in a power-law fashion as $M^{0.64}$, consistent with a constant Jeans mass for the clumps (Bertoldi & McKee 1992).

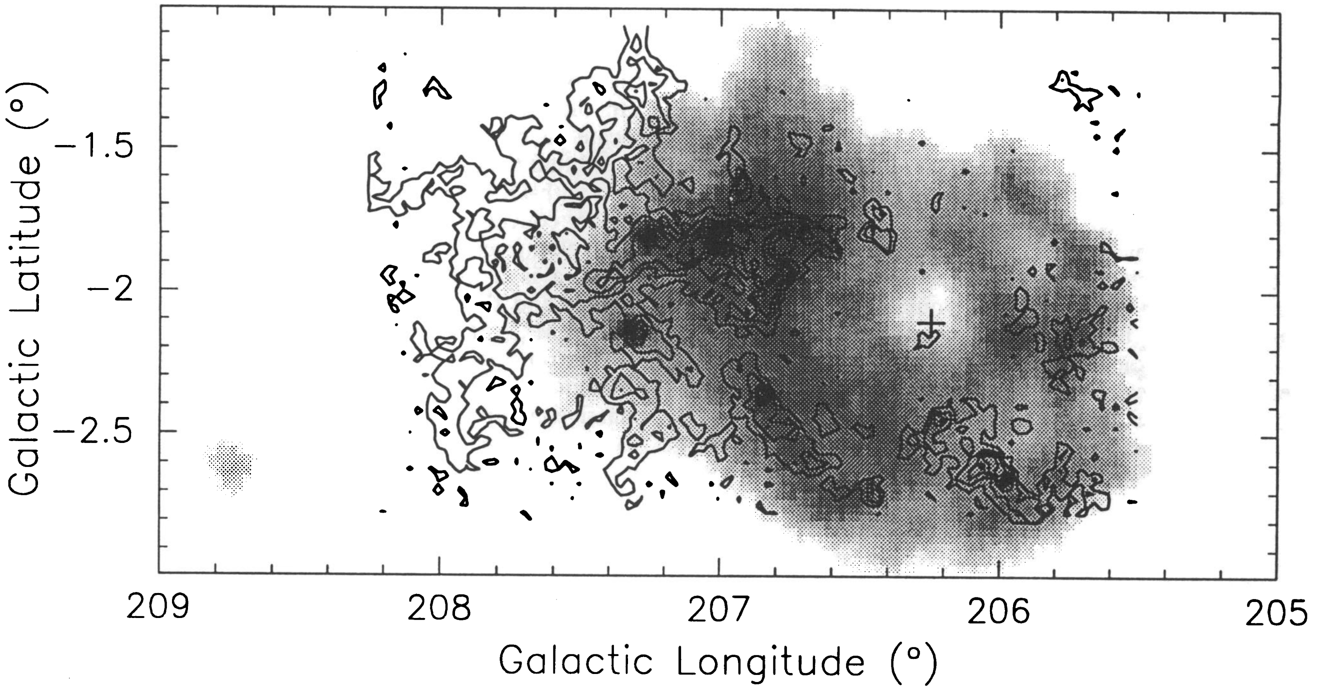

FIG. 17.—*IRAS* 100 μm emission associated with the RMC. The infrared emission is presented as a logarithmic halftone, varying from 100 to 1000 MJy sr^{-1}, overlaid on a velocity integrated map of the CO emission (contoured as in Fig. 1).

and clump mass implies (or is a result of) constancy of the clump Jeans mass. Figure 16 confirms this result: the least-squares fit implies a power-law relation, $R\sigma_v^2/GM \propto M^{-0.64}$, and therefore, $M_{\rm Jeans} \propto M(R\sigma_v^2/GM)^{3/2} \simeq$ constant. Particularly for the low-mass clumps, the correlation is rather weak, and in practice there is some scatter in the measured value of $M_{\rm Jeans}$ for each clump. Interestingly, however, the average value, $\langle M_{\rm Jeans} \rangle = 1100\ M_\odot$, is close to the maximum clump mass in the cloud (Fig. 9).

Star formation in the RMC, therefore, is occurring only in the most massive clumps for which gravity dominates the dynamics. It should be noted, however, that because of the distance to the RMC, the *IRAS* results are complete in this cloud only to a luminosity $L_{\rm min} \simeq 100\ L_\odot$; lower luminosity stars or stellar aggregates may be forming elsewhere. With this proviso, Figures 9 and 16 show that high mass and gravitational boundedness are not by themselves sufficient conditions for star formation to take place: there exist some massive, gravitationally bound clumps that are not associated with an *IRAS* source. We show in the next section that one must also consider the location of the clumps in the cloud.

4.4. *Variations of Clump Properties across the Cloud*

The H II region NGC 2244 (the Rosette Nebula) contains four O stars and 13 B stars and is centered at $l = 206\overset{\circ}{.}247$, $b = -2\overset{\circ}{.}106$ (Celnik 1983). With a luminosity of $2 \times 10^6\ L_\odot$, 2 orders of magnitude greater than that of any of the embedded sources, it clearly represents the major recent star-forming event in the RMC. The *IRAS* 100 μm skyflux plate of the region (Fig. 17) shows strong emission from heated dust around the H II region (but a minimum at the center indicating dust destruction or expulsion close to the stars). There is evidence for an expanding H I shell (Kuchar & Bania 1993) that, coupled with the morphology of the *IRAS* and CO emission, demonstrates the heating, dissociating, and dynamical effect of the stars. The *IRAS* emission extends well into the cloud suggesting that the effect of the H II region may not be just local. It is possible to gauge its influence by comparing the conditions of clumps on different sides of the cloud. In this subsection we measure how clump properties change as a function of the distance, $d_{\rm H\,II}$, from the H II region.

Motivated by Figure 17, which appears to show greater CO brightness temperatures closer to the center of the H II region than further away, and Figure 14, which shows that the most luminous *IRAS* sources are clustered around the H II region, we looked for gradients of clump excitation temperature and star-formation activity with $d_{\rm H\,II}$. Figure 18 plots the excitation temperature for each clump against $d_{\rm H\,II}$. The data have been binned in equal logarithmic distance intervals to show the

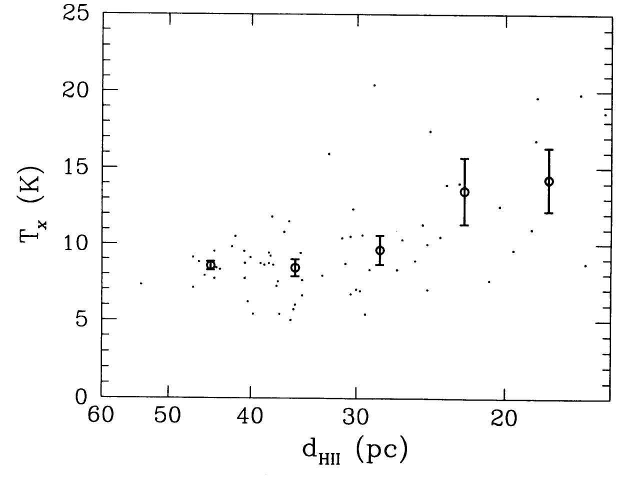

FIG. 18.—Variation of excitation temperature across the cloud. Clump excitation temperatures are plotted as a function of their distance from the center of the Rosette Nebula. The data are binned and the mean temperature, with dispersion about the mean, are indicated by the large open circles and error bars.

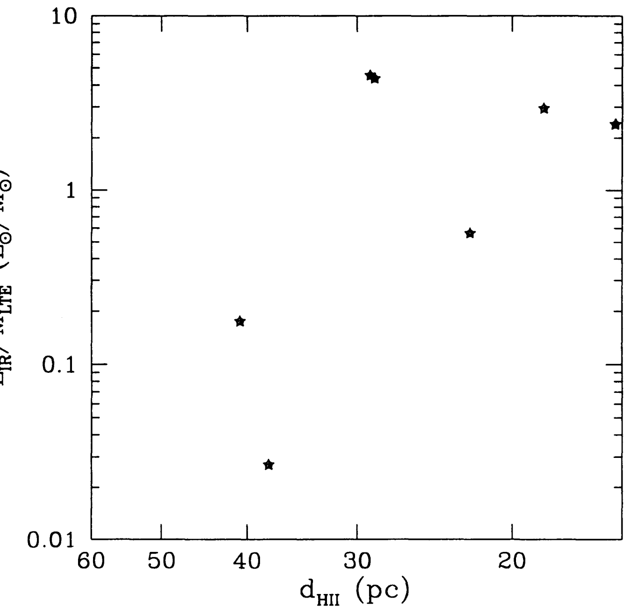

FIG. 19.—Variation of star-formation efficiency across the cloud. There are seven clumps in the ^{13}CO map that are associated with *IRAS* sources. For each of these clumps the infrared luminosity of the embedded source divided by the clump mass, a measure of the efficiency with which the clump is forming stars, is plotted against the distance of the clump from the center of the H II region.

trend better: the average T_{ex} increases by almost a factor of 2 for clumps close to the H II region compared to clumps on the far side of the cloud. For the star-forming clumps, the ratio L_{IR}/M is a measure of the star-formation activity within that clump. Figure 19 demonstrates that $L_{IR}/M \simeq 1$ for $d_{H\,II} < 30$ pc, but decreases by almost an order of magnitude for the two more distant star-forming clumps.

We have looked for variations in the clump masses, sizes, and line widths across the cloud, but have found no significant gradients. The average clump density, plotted in Figure 20 (binned in the same way as Fig. 18) is slightly greater, however, by about a factor of 2, for $d_{H\,II} \lesssim 30$ pc than further away.

We have identified, therefore, three gradients in clump properties across the cloud; clump excitation temperature, star-formation efficiency, and average density. These three quantities all increase with increasing proximity to the H II region. This is suggestive that the stars in the Rosette Nebula have a major effect on the rest of the cloud, by heating and compressing them (Bertoldi 1989) and increasing the star-formation efficiency within them (Elmegreen & Lada 1977). Alternatively, the cloud may have formed in a nonuniform manner and these gradients simply reflect earlier preexisting conditions of the cloud. If so, then the clumps closer to the H II region (and the original clump that formed the stars in the H II region) may have formed either earlier or may be more predisposed to star-formation than the clumps on the opposite side of the cloud. That is, the observed gradients are the result of an age or evolutionary gradient in the cloud itself.

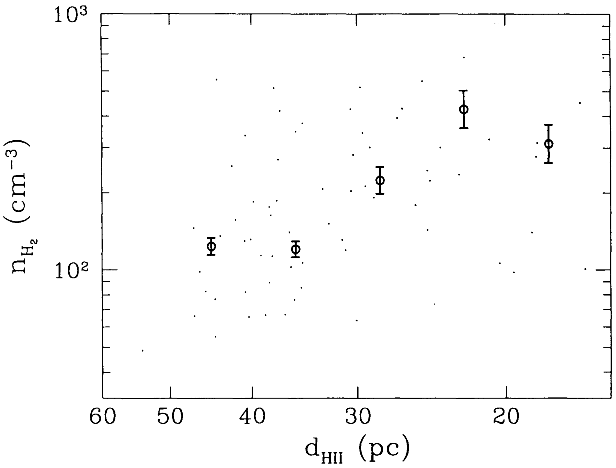

FIG. 20.—Variation of clump average density across the cloud. Clump average densities, defined as in Fig. 15 are plotted against their distance from the cloud. The data are binned as in Fig. 18.

Perhaps the most significant result is that these gradients exist. If similar patterns are observed in other clouds, it will be strong evidence that star formation is not a purely local phenomenon and proceeds in a rather systematic way through a cloud, rather than occurring at random, unrelated places within a cloud. The question of the cause or effect of such gradients could then be addressed.

4.5. *Clump Profiles*

Most of the clumps in Table 2, certainly all the massive ones, are several times larger than the beam (Fig. 3). Since the Clumpfind algorithm extracts clumps from the data cube using only the contours to guide it, there is no imposed or preferred shape to the clumps that are found, and therefore the data can be used to determine the actual clump density profiles.

The clump finding technique effectively isolates each clump from the data cube. For each line of sight through the clump $N_{^{13}CO}$ may then be calculated in the manner described in § 3. We first note that the clump peak column densities span a factor of about 30 and vary with clump mass as $N_{peak} \propto M^{0.62}$ (Fig. 21). The seven star-forming clumps all have high peak column densities, $N_{H_2} \simeq 10^{22}$ cm^{-2}. N_{peak} is used to normalize

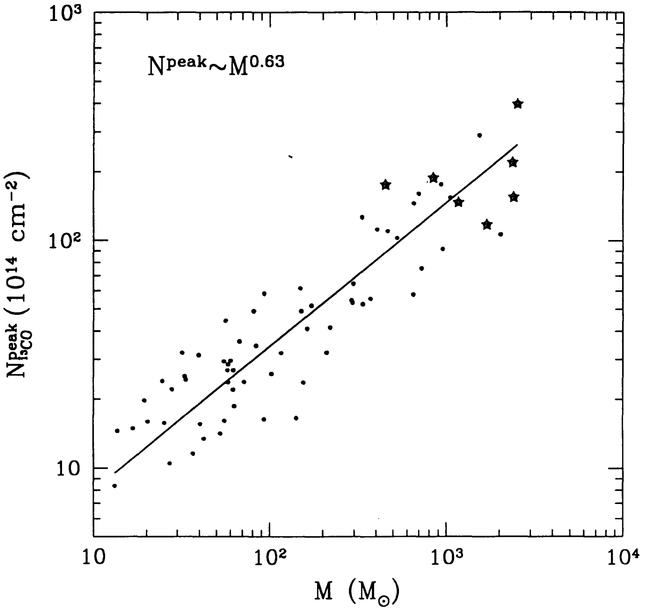

FIG. 21.—Variation of peak (central) column density of ^{13}CO as a function of the clump mass. The straight line indicates the least-squares fit to the power-law exponent relating the two indicated in the top left hand corner. The asterisks (*) correspond to the clumps associated with an *IRAS* source.

the column densities for each clump so that their profiles can be considered together on the same scale.

Since the clumps are observed to have small aspect ratios and are, to first order, spherically symmetric, the profiles have been radially averaged. Consecutive annuli are created around the peak of each clump and averages are calculated at all radii where the clump accounts for at least 50% of the total number of pixels in that annulus. We have varied this percentage and find that, if higher, the spatial range over which the profiles are defined becomes too small to be useful, and if lower, the determination of the profile at large radii is subject to errors due to small number statistics. We have also verified our procedure by running tests on simulated clouds consisting of clumps with known density profiles (see WGB).

The result of this analysis is a set of points $[r, N_{^{13}\mathrm{CO}}(r)]$ defined for two to five points for each clump. The conclusions of this section are derived from the analysis of those clumps with adequate sampling (at least four points) and dynamic range (more than a factor of 3 in each axis) for which the density profile can be reliably determined. We have attempted to fit the density profiles to three different functional forms; Gaussian, exponential, and power-law[1] by plotting log $N_{^{13}\mathrm{CO}}(r)$ against, respectively, r^2, r, and log $(1 + r/a)$. None of the profiles fall off fast enough to fit a Gaussian or an exponential, and a power law seems most appropriate. In addition, there are noticeable trends in the steepness of the average profiles for clumps that are pressure bound, gravitationally bound, and star forming. Normalized column density profiles of each clump and their averages are plotted in Figure 22.

We have considered different values for the core radius, a, but have restricted it to be no greater than the beam size, since the column density falls off rapidly one beam away from the peak. In fact, the averages are best fit to a power law for $a \simeq 0.7$ pc, equal to the beam size, suggesting that the central parts of the profile are unresolved. The individual profiles show some dispersion, but for the most part seem to follow a power-law decline quite well. The average profiles in the second panel show the power-law variation and deviations from it more clearly. The column density falls off more slowly for the pressure-bound clumps than it does for the gravitationally bound clumps that, in turn, fall off more slowly than the star-forming clumps. The least-squares fits to the power-law exponent, n, where $N(r) = N_{\mathrm{peak}}(1 + r/a)^{-n}$ are 0.81 (pressure bound), 1.05 (gravitationally bound), and 1.18 (star forming), all close to 1.0, the projection of the density profile of an isothermal clump, $\rho(r) \propto r^{-2}$.

Figure 21 shows that the peak column densities are greater for the star-forming clumps, and the optical depth may well be higher for these clumps at the center. Such an effect would tend to flatten the observed profile, and it is possible, therefore, that the actual difference in steepness of clump profiles between star-forming and non–star-forming clumps is underestimated. The strong CS emission (see § 4.3) observed in the star-forming clumps is additional evidence that their profiles may be steeper than indicated here.

It might be expected that the radial density profile of a non–self-gravitating clump would be flatter than that of a self-gravitating clump, but the difference between the two is surprisingly small: if the non–self-gravitating clumps are bound by external pressure, as we argue in § 4.7.2, one would expect that the pressure within the clumps would be nearly constant, especially in those clumps where the pressure due to gravity is a small fraction of the pressure due to bulk motion. In this case, the density within a clump should be constant and the column density profiles would be a reflection of geometry

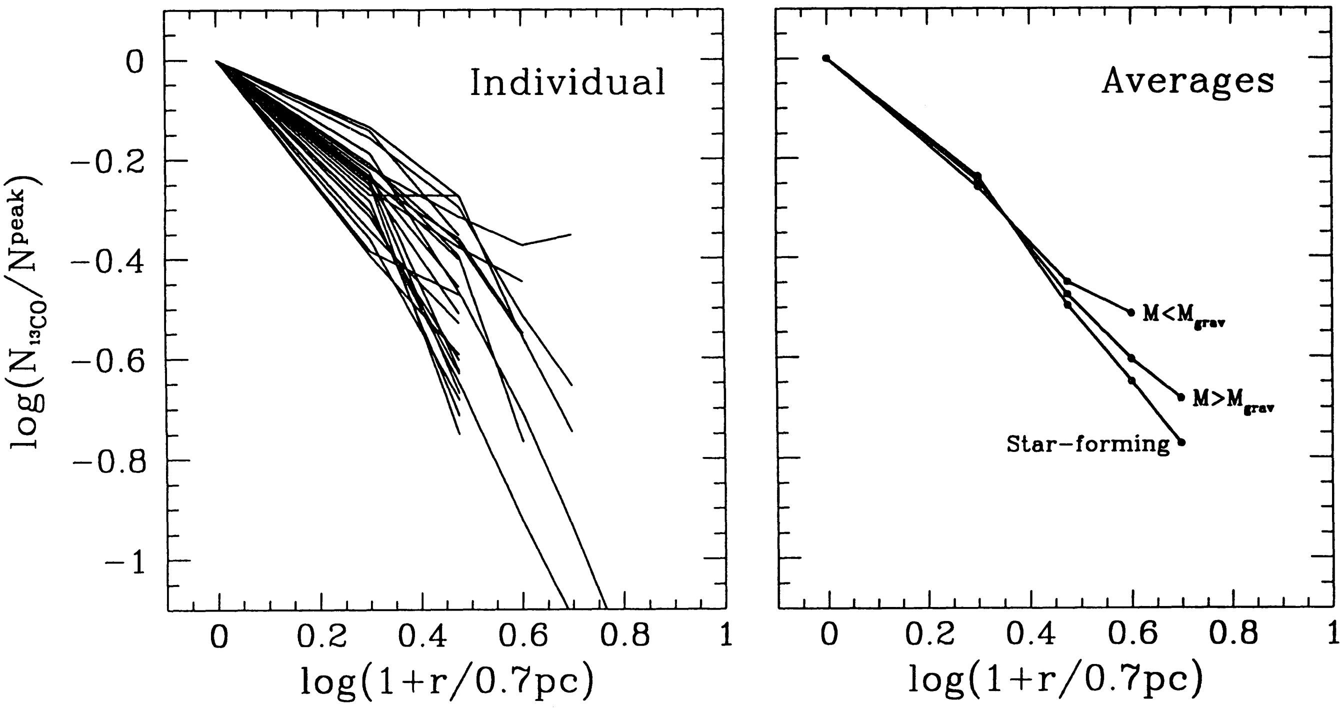

FIG. 22.—Clump column density profiles. The radially averaged column density of ^{13}CO, normalized by its peak value, is plotted as a function of distance from the clump center for each clump. The left panel shows the profiles for all the clumps in the catalog, and the right panel shows the average profiles for those clumps that are pressure bound ($M < M_{\mathrm{grav}}$), gravitationally bound ($M > M_{\mathrm{grav}}$), and star forming.

---

[1] Not a strict power-law, $N(r) \propto r^{-n}$, which diverges at the origin, but one softened by an additional parameter, a, the core radius.

only; nearly flat at the center and very steep at the edges. This is very different from what is observed either in Figure 22 or in contour maps. The radial profiles of the pressure-bound clumps suggest rather, that if they are isobaric, they have density gradients within them, with density increasing toward the center. This situation would arise as the result of a velocity dispersion or temperature gradient within the clumps; the clumps are either most quiescent or coldest near their centers. Such a situation may result from external UV heating due to the ambient radiation field (in this case, dominated by the H II region). We show in § 4.6.2 that the observed line widths of all of the clumps are significantly larger than one obtains from any reasonable estimate of the kinetic temperature. More likely, then, the increased central density in the pressure-bound clumps is accompanied by a somewhat decreased velocity dispersion. The observed dispersion comes from gas all along the line of sight, however, and it may not be apparent unless one had both high-resolution and high-sensitivity observations of the pressure-bound clumps to confirm this picture.

Finally, again one must add a cautionary note about substructure within the clumps. Small, unresolved knots of dense gas may well exist in some of the clumps, particularly those forming stars; high-resolution observations with a higher density tracer such as CS may show profiles that are not nearly as smooth, or radially symmetric. This does not alter the conclusion, however, that the average column density of the more moderate density gas traced by ^{13}CO decreases in an approximately power-law fashion, and that the decrease is steepest for the star-forming clumps.

4.6. *The Relationship between the Atomic and Molecular Gas*

The density of molecular hydrogen in the RMC averaged over the volume of the entire cloud is 17 cm^{-3}, a factor of 13 less than that found for the mean density of individual clumps (see Fig. 15); as discussed in § 4.2.4, the volume filling fraction of the clumps is therefore only 8%. What is the interclump medium that makes up the remaining 92% of the volume of the cloud?

We have already argued in § 4.1.2 that the Clumpfind algorithm assigns most of the ^{13}CO emission to clumps, so the discrepancy in clump and cloud densities is not an artifact of the clump finding method. It is worth noting, however, that the cloud average CO spectrum in Figure 4 shows extended, low-level wings that may signal the presence of an extended molecular component (Blitz & Stark 1986). Moreover, precise estimates of the amount of H_2 would be very difficult to make from observations of CO, and especially ^{13}CO, if the molecular gas is very diffuse (Reach, Koo, & Heiles 1994), for then the column density may be insufficient to allow the formation of CO. Evidence against the existence of large amounts of diffuse molecular gas comes from C II observations of molecular clouds (e.g., Howe et al. 1991; Stutzki et al. 1988) that show that far-UV radiation penetrates deeply into the cloud. Such radiation would photodissociate the low-density molecular interclump gas. Nor can the interclump medium be highly ionized because of the strong Hα emission that would then be observed (e.g., Block et al. 1992), and that would quickly cool down the gas. The interclump medium, therefore, is expected to be predominantly atomic.

Atomic gas can be readily observed with the 21 cm H I line, and has been mapped in the vicinity of the RMC by Kuchar & Bania (1993). The angular resolution, 4′, and the velocity resolution, 0.5 km s^{-1}, are comparable to the molecular observations. Unlike CO, H I is ubiquitous and is observed along every line of sight at these low Galactic latitudes. It is significant, therefore, that the H I observed in the direction of the RMC is centered on the velocity of the cloud and drops off sharply within ±10 km s^{-1} of the CO emission. Thus, although there is undoubtedly unassociated H I in the foreground and background of the cloud, it would appear that much of the H I that is observed toward the RMC is associated with the cloud.

Figure 23 plots contours of the CO emission overlaid on a gray-scale image of the H I emission, integrated over the same velocity range, $v = 5 - 25$ km s^{-1}. There are two primary peaks in the H I that occur on the edges of the CO maps, giving the appearance of an atomic shroud around the molecular cloud. Similar atomic envelopes have been observed around a number of molecular clouds (Wannier et al. 1991; Andersson & Wannier 1993; Blitz 1993). With these high-resolution observations, however, we can pursue the relation of the atomic to molecular gas down to the scales of the clumps in the cloud. Figure 24 plots CO channel maps over H I gray-scale maps of the central region of the cloud at nine sequential velocities. although there is H I generally associated with the CO, there is a detailed anticorrelation between the two species, the CO maxima occurring at H I minima and vice versa. Again, the persistence of this association with velocity demonstrates that the two gaseous phases are coupled. Spectra of H I, CO, and ^{13}CO toward four different positions within the cloud are displayed in Figure 25. These spectra complement the maps by showing the overall atomic envelope around the molecular gas and also the detailed anticorrelation around the peaks of CO.

It is likely that the observed dips in the H I brightness temperature are due not to a real decrease in column density, but to absorption by cold H I associated with the molecular clumps. Self-absorption of H I around molecular gas has been observed both on the large scale (Burton, Liszt, & Baker 1978) and on the small (clump) scale (Feldt 1993). The magnitude of the absorption can be used to estimate the column density of the absorbing gas,

$$T_{\rm obs} = T_{\rm bg} e^{-\tau} + T_s(1 - e^{-\tau}) ,$$

$$N_{\rm H\,I} = 1.8 \times 10^{18} T_s \tau \Delta v .$$

At the absorption centers, the observed H I brightness temperature, $T_{\rm obs} \simeq 28$ K, and the background brightness temperature is $T_{\rm bg} \simeq 40$ K (estimated from positions without absorption). We take the spin temperature of the cold, absorbing gas to be about the same as the molecular gas, $T_s \simeq 10$ K. This results in $\tau \simeq 0.5$, which, for a line width $\Delta v \simeq 2$ km s^{-1}, implies a column density $N_{\rm H\,I} \simeq 2 \times 10^{19}$ cm^{-2}. This is 2 orders of magnitude less than the column density of H_2 through the associated clump, and we conclude that the cold ($T_s \simeq T_{\rm CO}$) H I can only amount to a few percent of the total gas column density through the clump. Feldt's (1993) more careful analysis results in the same conclusion.

The small fraction of absorbing atomic gas does not significantly change the overall picture: the velocity structure and overall morphology of the non–self-absorbing gas demonstrate that there is a large amount of atomic gas intimately associated with the cloud and the clumps within it. There are, however, a number of positions in the cloud where there appears to be H I absorption but no detectable CO emission. The transition from H I to H_2 begins at such low column densities that CO does not survive (Hollenbach, Takahashi, & Tielens 1991) so it

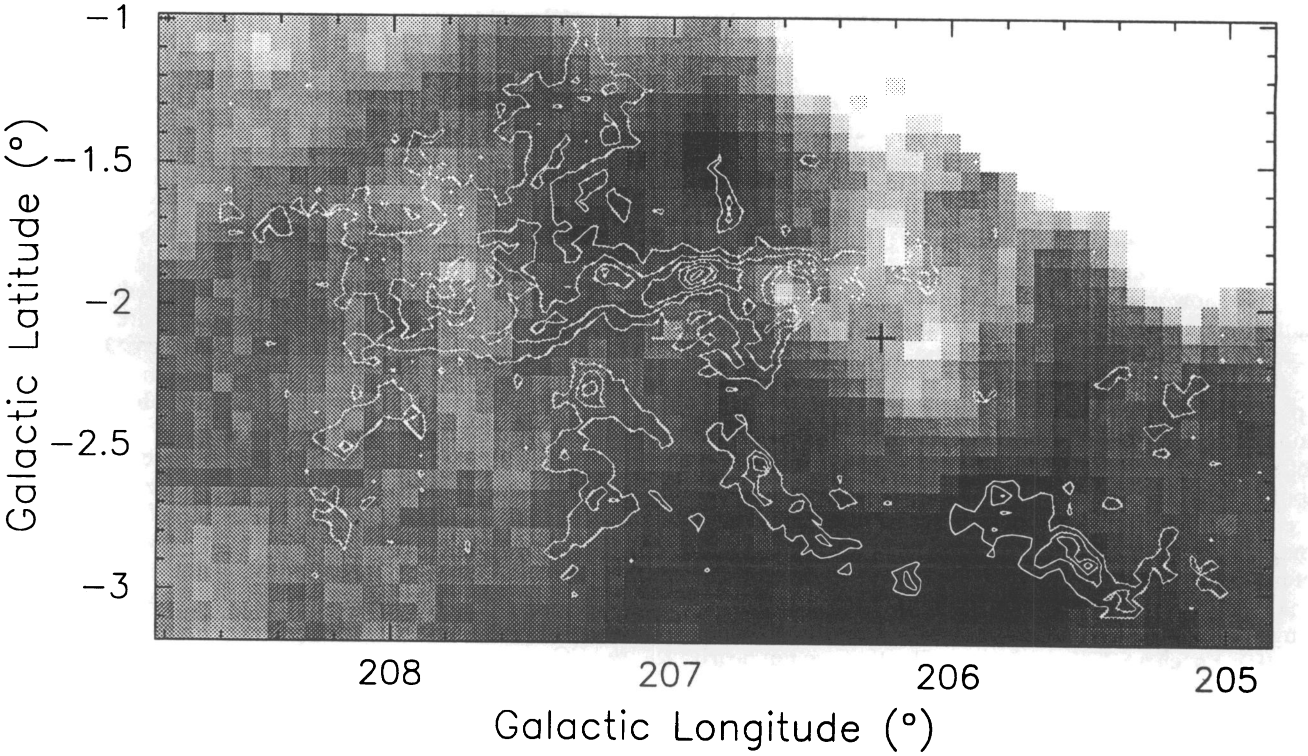

FIG. 23.—Atomic hydrogen associated with the RMC. H I observations by Kuchar & Bania (1994) are presented in halftone with CO contours overlaid to show the relationship between the atomic and molecular gas. Both are velocity-integrated maps over the same range, $v = 5\text{–}25$ km s^{-1}. The H I halftone varies from 450 (*light*) to 620 K km s^{-1} (*dark*), and the CO contours from 15 to 120 K km s^{-1} in steps of 15 K km s^{-1}. The column density of H I is greatest at the edges of the CO emission; the atomic gas appears to shroud the cloud.

is possible that, along these lines of sight, there may be small or diffuse molecular clumps with little or no CO emission.

The dynamic range of the H I is far less than the CO in the above maps. This is to be expected if our association of the H I with the interclump medium is correct, for then the atomic gas would occupy over 90% of the volume of the cloud and would show far less contrast than the molecular gas that is concentrated into clumps filling less than 10% of the volume of the cloud. Integrating over the average spectra of each species imply average column densities

$$\langle N_{\rm H\,I}\rangle \simeq 1.3 \times 10^{21}\ {\rm cm}^{-2}\ ,$$

$$\langle N_{\rm H_2}\rangle \simeq 4.0 \times 10^{21} \mathscr{R}_{\rm RMC}\ {\rm cm}^{2}\ .$$

The quantity $\mathscr{R}_{\rm RMC}$ is the ratio of the CO to H_2 conversion factor in the RMC to the Galactic ratio, defined in § 4.1.1, and may be as small as 0.5. On the other hand, the H I is more extended than the CO (see for example the map in Blitz 1988), and some of the gas is foreground and background emission. We may estimate from that map that the mean $N_{\rm H\,I}$ above the background is 6×10^{20} cm^{-2}, about 50% of the total column along the line of sight. With this correction, summing over the area of the cloud implies the total mass of H I associated with the RMC is equal to $M_{\rm H\,I} = 5 \times 10^{4}\ M_{\odot}$.

4.6.1. *The Density Contrast between the Clump and Interclump Medium*

We are now in a position to estimate the density contrast between the clumps and the gas between the clumps. First, we found that Clumpfind assigned 89% of the ^{13}CO emission to individual clumps, and that 24% of the emission was below the $2T_{\rm rms}$ contour. If we assume that all of the unassigned emission is in a diffuse molecular component and that half of the emission below $2T_{\rm rms}$ is also diffuse, then 23% of the molecular gas is not assigned to clumps. If this gas is uniformly distributed within the volume of the cloud, then the mean diffuse molecular gas density is 3.5 cm^{-3}, probably a high estimate.

The mean atomic gas density is somewhat harder to estimate. An upper limit can be obtained by assuming that all of the emission we see in the direction of the RMC is within the volume of the molecular cloud. In that case, the mean H I density is given by the total average column density that we calculated above divided by the mean depth of the cloud, $L = A^{1/2} = 47$ pc, and comes to 9.0 cm^{-3}. On the other hand, if we take the excess above the background, 6×10^{20} cm^{-2}, over its full extent $\simeq 4°$ estimated from the map in Blitz (1988), we find $\langle n_{\rm H\,I}\rangle = 1.7$ cm^{-3}. Therefore, we can take $\langle n_{\rm H\,I}\rangle = 4$ cm^{-3} to within a factor of 2. Interestingly, the mean H I and H_2 density in this diffuse gas would be about the same, which is what one might expect in a region in which the strongly molecular GMC is being shielded from the dissociating UV radiation.

We then obtain a mean density of nucleons, $\langle n_{\rm H\,I}\rangle + 2\langle n_{\rm H_2}\rangle \simeq 11$ cm^{-3}, in the interclump gas compared to 440 cm^{-3} in the clumps themselves, for a density contrast of about 40. The density contrast will be larger if we have overestimated the amount of diffuse molecular gas. We must realize, of course, that the true physical picture is more complex: the maps in Figures 23 and 24 show that the H I is not uniformly distributed, and there are likely to be density gradients even in the diffuse gas. Nevertheless, this idealized picture is instructive about how much denser the clumps are than the surrounding medium.

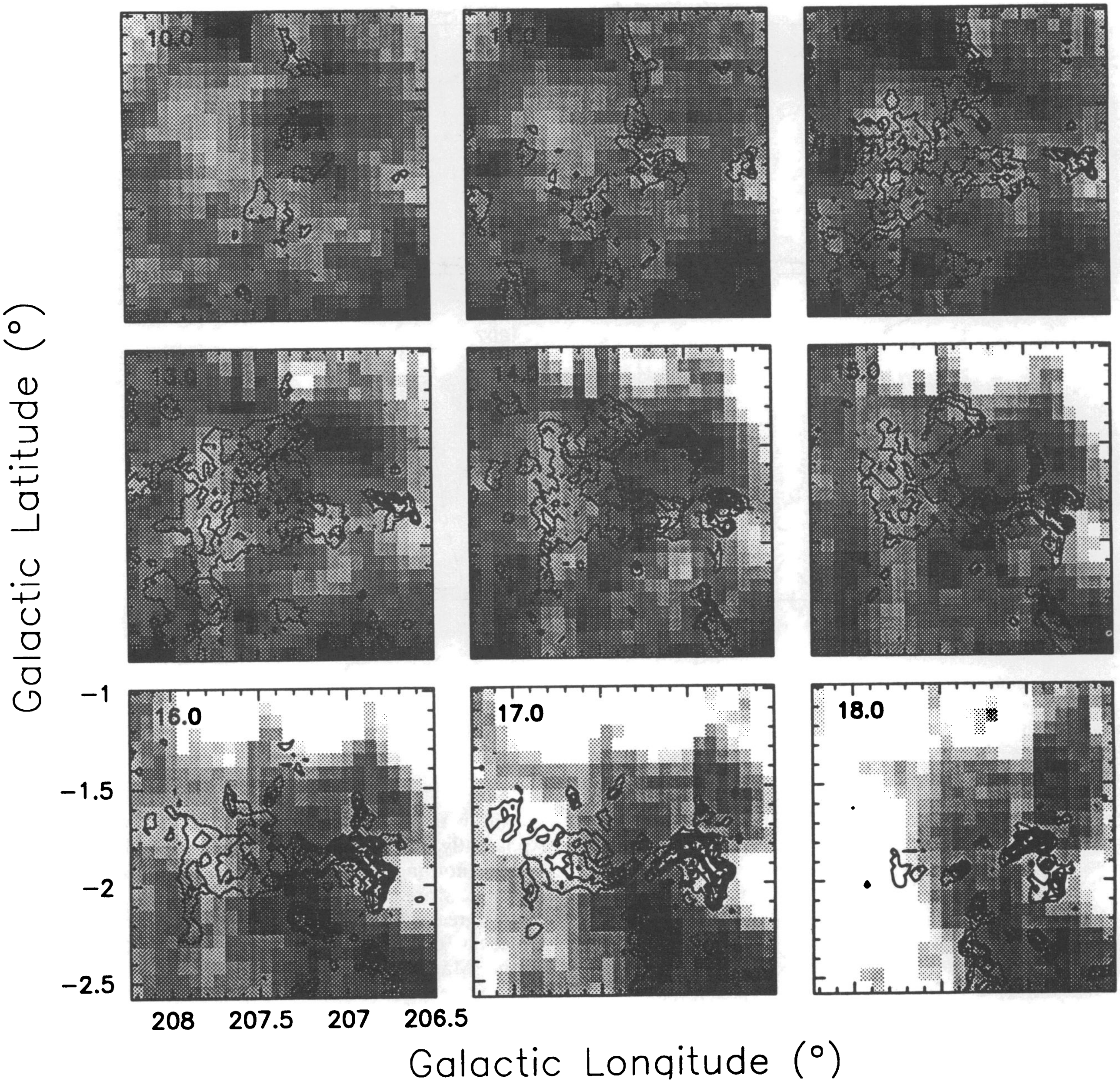

FIG. 24.—Channel maps of the atomic and molecular hydrogen toward the center of the RMC. Sequential slices through the H I and CO data cubes are compared over a range in velocity to show the detailed relation between the atomic and molecular gas. The H I is shown in halftone, from 25 to 37 K, with darker regions representing higher temperatures. CO contours start at 1.5 K, and are in steps of 1.5 K. Atomic gas is associated with the molecular gas down to the scales of the clumps that are seen here. There is again a tendency for the H I to peak away from the regions of CO emission.

4.6.2. *Pressure Equilibrium*

Even though the density contrast is high, the atomic gas can play an important role in the dynamics of the cloud. The pressure of the H I is sufficient to hold together those clumps in the cloud that are not self-gravitating. We determine the ram pressure of the H I and the turbulent pressure within a clump:

$$P_{\rm H\,I} = \rho_{\rm H\,I}\sigma^2_{v,\rm H\,I} ,$$

$$P_{\rm clump} = \rho_{\rm H_2}\sigma^2_{v,\rm H_2} .$$

The measured values for the densities and velocity dispersions are $n_{\rm H\,I} \simeq 4$ cm^{-3}, $\sigma_{v,\rm H\,I} = 10.5$ km s^{-1} for the H I, and $n_{\rm H_2} \simeq 220$ cm^{-3}, $\sigma_{v,\rm H_2} = 0.7$ km s^{-1} for the unbound clumps. Note that the observed line widths are highly superthermal even for the pressure-bound clumps; $(kT/m_{\rm CO})^{1/2} = 0.08$ km s^{-1} for a kinetic temperature $T = 20$ K. The derived values for the pressures are

$$P_{\rm H\,I}/k \simeq 5.3 \times 10^4 \ {\rm K\ cm^{-3}}$$

$$P_{\rm clump}/k \simeq 2.6 \times 10^4 \ {\rm K\ cm^{-3}} ,$$

in rather good agreement considering the uncertainties. Hence, the ram pressure of the H I can balance the turbulent pressure of the gravitationally unbound clumps.

We note that these pressures are greater than the total (thermal + magnetic + cosmic ray) pressure of the ISM. How are these pressures maintained? The RMC is self-gravitating and is therefore isolated from the requirements of pressure

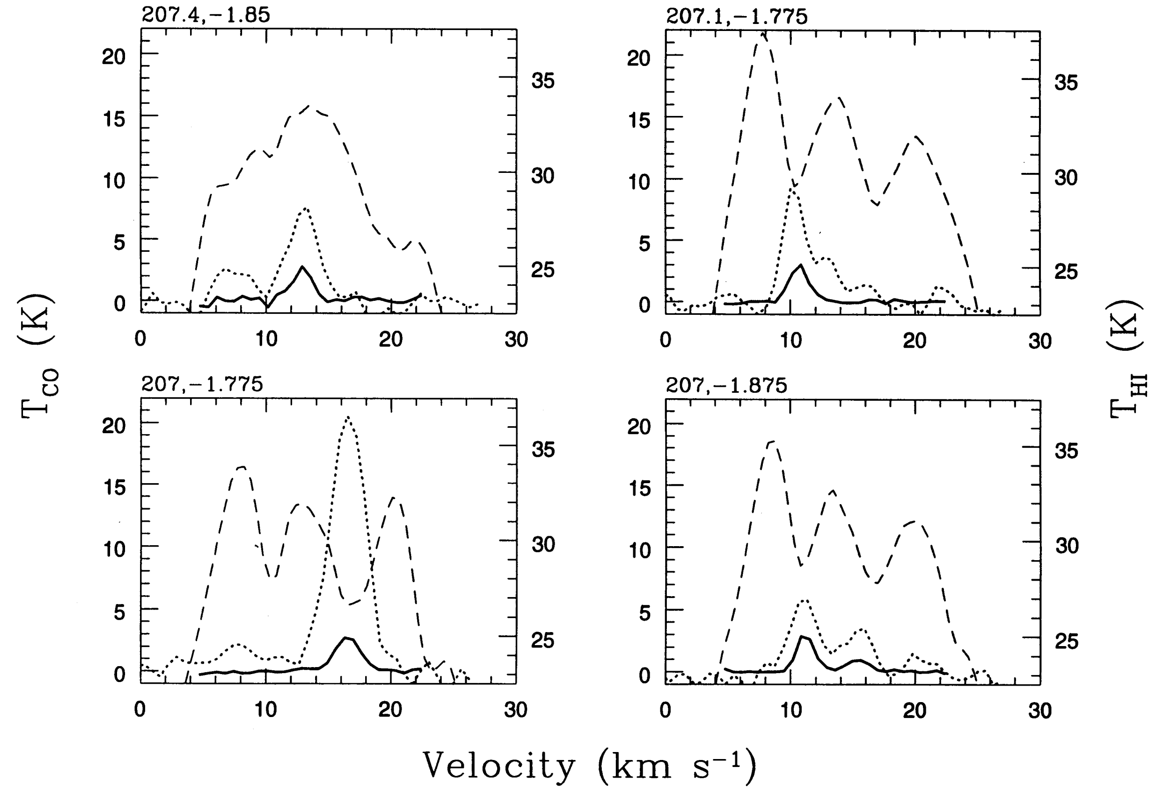

FIG. 25.—Spectra of H I, CO, and ^{13}CO in the RMC. Four representative spectra at positions indicated at the top of each panel are shown here. The ^{13}CO spectrum is the heavy, solid line, the CO spectrum is the dotted line. The temperature scale for these two are on the left-hand side. The H I spectrum is the dashed line, with the temperature scale on the right-hand side of each plot.

equilibrium with the general ISM. The pressure due to its gravity is

$$P_{\rm grav} = 2\pi\alpha_p G\Sigma_g^2 \ ,$$

where α_p is a factor near unity that depends on the geometry (Spergel & Blitz 1992). Using values from § 4.1, we find $\Sigma_g = 73\mathcal{R}_{\rm RMC}\ M_\odot\ {\rm pc}^{-2}$, and $P_{\rm grav}/k = 7.0 \times 10^5\mathcal{R}_{\rm RMC}^2$ K cm^{-3}. For $\mathcal{R}_{\rm RMC} = 0.5$ and $\alpha_p = 1$, $P_{\rm grav}/k = 1.8 \times 10^5\mathcal{R}_{\rm RMC}^2$ K cm^{-3} in very good agreement with the above estimates of $P_{\rm H\,I}$ and $P_{\rm clump}$. Viewed in this way, the interclump gas acts as a medium to transport the pressure due to the self-gravity of the cloud as a whole down to the scale of the smallest, gravitationally unbound clumps.

5. IMPLICATIONS FOR CLOUD EVOLUTION

The characterizations of the clumps made in § 4 have made it possible to learn something about the dynamical state of the cloud, which in turn makes it possible to learn something about the evolution of the cloud and how it forms stars: the ultimate aim of this study. Consider first the power-law slope of the clump mass function discussed in § 4.2.1. At some level within a molecular cloud, one expects that the mass spectrum of star-forming clumps will mirror the stellar IMF. We see clearly that the power-law index is far from the Miller-Scalo or Salpeter IMF, and so the natural conclusion is that either the clump mass function has nothing to do with the IMF or that it somehow evolves into the IMF. We note first that the mass function for clouds in which little star formation is currently taking place, such as the Maddelena-Thaddeus cloud (WGB), is, within the uncertainties, the same as that for the RMC. Apparently, the evolutionary state of a molecular cloud has little or nothing to do with the mass spectrum of the clumps within it. More to the point, the mass function for clumps with masses greater than about 0.3 $M_\odot$ in MBM 12, a high-latitude molecular cloud that does not appear to be gravitationally bound (Magnani, Blitz, & Mundy 1985), has a similar slope to that of the RMC. If the clumps, which are themselves not bound by gravity in this cloud and seem unlikely ever to form stars, have the same mass function as a GMC that does form stars, it would be surprising if the IMF, which does require gravity, had anything to do with the clump mass function.

Furthermore, the individual clumps are not in general forming individual stars. This follows from the known efficiency of star formation that is typically a few percent averaged over an entire molecular cloud (Myers et al. 1986). Because star formation in the RMC is largely confined to the most massive clumps, many stars must be forming within the individual clumps if the star-formation efficiency of the RMC is typical of that of other GMCs. This conclusion is confirmed by direct infrared imaging, which shows that the clumps are forming small clusters or stellar aggregates (Phelps & Lada 1995). Since a single clump in Table 3 that forms stars does not form a single star but a *group* of stars, there is no reason why the ensemble of clumps should mirror the IMF that is presumably formed *within* a single clump.

Where, then, do we look for the progenitors of the stellar IMF? Apparently, we must find it within the structure of the individual star-forming clumps in Table 2. That is, these clumps must ultimately develop substructure, and it is from that substructure within the gravitationally bound, star-forming clumps that the IMF is generated. The substructure may be better manifested in higher density gas tracers such as CS or HCN.

That the clump collision time is short compared to the age of the stars in the complex (Blitz & Shu 1980, and references therein) suggests that dynamical evolution of the clump ensemble should have taken place. The measurements of the clump velocity dispersion and the positional dispersion from the midplane as a function of mass both are consistent with the inferred dynamical evolution. Since the velocity dispersion of the clump ensemble is large compared to the sound speed in the clumps, collisions between them should be highly inelastic, though fragmentation may also occur. All of this implies that the clumps should grow by a process of collisional agglomeration, and that the mass spectrum of the clumps should be a function of the age of a cloud. The comparison between the mass spectrum of the RMC and the Maddalena-Thaddeus cloud (WGB) is therefore surprising in that it shows no significant difference between the mass spectra of the two clouds. Even more surprising is that the spectrum of clumps for clumps greater than 0.3 $M_\odot$ for a GMC that is not gravitationally bound (MBM 12; Pound 1994), also has about the same slope. Here is a cloud that may be so young (Magnani et al. 1985) that it is not even clear the clumps have interacted. How can the idea of clump agglomeration be reconciled with the observations that suggest a constancy of the mass spectrum?

There are many examples in nature of collisional processes acting on a group of objects that results in a power-law distribution of sizes and masses. Specific examples include ash, sand, rocks, meteorites, asteroids (Hartmann 1969, and references therein), planetary ring systems (Esposito & Colwell 1989), and interstellar dust (Mathis, Rumpl, & Nordsieck 1977). In each case, the index of the mass spectrum is, or is very close to, -1.5. The mass spectrum may evolve through further collisions in a statistical manner first described in an astrophysical context by Field & Saslaw (1965). Detailed calculations (see, e.g., Lissauer & Stewart 1993, and references therein) suggest that agglomerational processes do not change the slope of the mass spectrum, but rather the most massive particles at the end of the distribution. Similarly, one might imagine that the clump mass spectrum in a cloud evolves through a series of agglomerations from the lowest masses to the highest such that the maximum clump mass increases, while clump numbers decrease, in a manner that preserves the slope and total mass. There can be no analogous result to the runaway effect that is seen in planetesimals, however, because our observations suggest that once a clump reaches a certain mass, $M \approx 10^3\ M_\odot$, star formation is almost inevitable. The consequent breakup of the massive clumps may replenish the low-mass end of the distribution. In this picture, star formation is the limiting factor in determining the mass of the largest clumps in a molecular cloud.

Synthesizing what we have learned from the other observations presented in this paper, we suggest the following tentative picture for the formation and evolution of a GMC. A neutral atomic hydrogen cloud with a column density in excess of 10^{21} cm^{-2} can shield dissociating UV radiation and permit the formation of molecules. This process may be occurring at some of the locations in the RMC where there are absorption dips but no detectable CO. If this is the case, there appears to be a significant temperature drop associated with the formation of H_2, which would lead to a corresponding decrease in pressure. Dense molecular clumps form, and the residual atomic gas becomes the interclump medium. Excess kinetic energy may be radiated away in clump collisions that allow the cloud as a whole to become more gravitationally bound, and for its internal pressure to increase and rise above that in the general ISM. This hydrostatic pressure can support the low-mass clumps that are not self-gravitating. The masses of the largest clumps increase through collisions with other clumps, in a manner that preserves the mass spectrum as we have described above. Small clumps are nevertheless constantly regenerated as the fragmented byproducts of collisions and the action of newly formed stars. The most massive clumps sink toward the center of the gravitational potential well of the cloud: in position about its midplane, and in rotation about its systemic velocity. When enough gas gathers together in one clump, star formation is inevitable and the clump is destroyed. The impact of massive star formation within, or near to, a cloud may result in clump compression, possibly triggering further star formation in it. Ultimately, the stars that the cloud forms dissociate and eventually destroy it.

6. SUMMARY

We have presented a detailed analysis of the structure of moderate density, $n_{H_2} \simeq 10^3$ cm^{-3}, gas in the RMC. This work was based primarily on observations of ^{13}CO, because of its optical thinness, but CO observations were also used to find excitation temperatures of the clumps.

Comparison of the summed emission of the CO and ^{13}CO over the region of the ^{13}CO mapping showed that standard Galactic values for the conversion factors between N_{H_2} and W_{CO} or $N_{^{13}CO}$ do not give consistent results. If $N_{H_2}/N_{^{13}CO} = 5 \times 10^5$, the value based on dust extinction measurements, consistency of mass estimates of CO, ^{13}CO, and (to a lesser extent) the gravitational mass, require

$$X_{RMC} = 1.1 \times 10^{20}\ \mathrm{cm}^{-2}\ (\mathrm{K\ km\ s}^{-1})^{-1}\ .$$

The clump mass distribution, $dN/dM \propto M^{-1.3}$, is similar to that measured for clumps in other clouds and is flatter than the mass distribution of field stars in the Galaxy. We have argued that the stellar IMF arises from processes within an individual clump, presumably the substructure within the star-forming clumps at smaller spatial scales and larger densities. The strongest CS emission in the cloud is associated with the star-forming clumps, which also have steeper density profiles than low-mass, pressure-bound clumps. The maximum clump mass may be limited by the inevitable formation of stars within it.

Dynamical information about the cloud was derived from the spatial and velocity characteristics of the clump ensemble. The mean clump velocities vary steadily across the cloud but the line of steepest gradient is not parallel to Galactic longitude (and is, therefore, unrelated to Galactic rotation). The energy contained in this large-scale ordered motion is dynamically insignificant compared to the kinetic energy of the overall motions of the clumps. The clumps are not, however, randomly positioned within the cloud; there is a clear segregation of the most massive clumps toward the cloud midplane. Similarly, the dispersion about the mean velocity gradient is smallest for the most massive clumps.

The PSC was used to locate the clumps that are sites of current star formation. The star-forming clumps were all massive and gravitationally bound, $M > M_{grav}$. In five out of the seven clumps $M > 2M_{grav}$, indicating that the clumps are virialized. These ^{13}CO properties by themselves could not, however, be turned into a criterion for predicting a priori which clumps are star forming: there are several massive, bound (even virialized) clumps that are not associated with an *IRAS* source. The principal difference between the massive, bound, star-forming clumps and the massive, bound, non–star-forming clumps is their location in the cloud, and, in particular, their proximity to the Rosette Nebula. The stars in the H II region lie toward the extremes of gradients in clump excitation temperatures, average densities, and star-formation efficiencies. It is not possible to say, from these data alone, whether the 17 OB stars in the H II regions are responsible for all or any of the observed gradients. Comparisons with other clouds will show how typical the situation in the RMC is, and whether star formation spreads systematically through a cloud or is more sporadic; the location of star-formation sites being independent of the star-formation history of a cloud complex.

The radial column density profiles of the clumps have been measured and seem to fit a power law best, though an exponential form is not entirely ruled out. The core radius of the power-law fit was set equal to the resolution of the observations and for both the power-law and exponential forms, the profiles become increasingly steep as one goes from pressure-bound to self-gravitating to star-forming clumps. The radial profiles are consistent with $\rho(r) \propto r^{-2}$ density profiles.

Molecules must form from atoms, so it is not surprising that the RMC, like other clouds, is surrounded by a neutral atomic envelope. The Kuchar and Bania observations show more than just that, however, and demonstrate that H I is closely associated with the molecular emission at the scales of the clumps in the cloud. In some places, at least, there is a very clear anti-correlation of H I and CO emission, in position and velocity, showing that the molecular and atomic gas are spatially and kinematically related, but mutually exclusive, and we identify the H I as the interclump medium. The ram pressure of the H I is comparable to the pressure due to the self-gravity of the cloud, and is sufficient to balance the turbulent pressure of the small, unbound clumps. There is no need, therefore, for there to be a constant state of clump "evaporation" and creation, despite their large internal line widths.

There are many signposts of the evolution from cloud formation to star formation that are contained within the density structure in a molecular cloud. Such signs are not, however, restricted solely to the molecular component: The OB stars in the Rosette Nebula may have a significant effect on the remainder of the cloud, as indicated not only in molecular gas properties, but also in the *IRAS* 100 μm skyflux plate measuring the hot dust, and the PSC showing the locations of star formation. Similarly, our study was enhanced by the Kuchar & Bania (1993) H I observations showing the detailed relationship between the atomic and molecular gas. Our understanding of the molecular cloud becomes more complete when, paradoxically, nonmolecular components are considered: the atomic gas from which the molecules form, and the stars—the end products of the density fluctuations that we set out to study.

We would like to thank Jurgen Stutzki for patiently refereeing our work again, and for his helpful comments. This research was partially supported by an NSF grant to L. B. and has made use of data obtained through the High-Energy Astrophysics Science Archive Research Center Online Service, provided by the NASA-Goddard Space Flight Center. We would particularly like to thank Tom Kuchar for making the Arecibo H I data available to us. Tamara Helfer took several $C^{18}O$ spectra while at the NRAO 12 m telescope. Chris McKee and Frank Bertoldi provided clarifying comments on an early version of the manuscript, and we have, in addition, enjoyed many pleasurable and informative discussions with Eugène de Geus, Carl Heiles, Frank Shu, and Marc Pound during the course of this work.

REFERENCES

Andersson, B. G., & Wannier, P. G. 1993, ApJ, 402, 585
Bash, F. N., Green, E., & Peters, W. L. 1977, ApJ, 217, 464
Bertoldi, F. 1989, ApJ, 346, 735
Bertoldi, F., & McKee, C. F. 1992, ApJ, 395, 140
Binney, J., & Tremaine, S. 1987, in Galactic Dynamics, ed. J. P. Ostriker (Princeton: Princeton Univ. Press), 190
Blitz, L. 1987, in Physical Processes in Interstellar Clouds, ed. G. E. Morfill & M. Scholer (Dordrecht: Reidel), 35
———. 1988, in Millimetre and Submillimetre Astronomy, ed. R. D. Wolstencroft (Dordrecht: Kluwer), 269
———. 1990, in The Evolution of the Interstellar Medium, ed. L. Blitz (San Francisco: ASP), 273
———. 1993, in Protostars and Planets III, ed. E. H. Levy & J. I. Lunine (Tucson: Univ. Arizona Press), 125
Blitz, L., & Shu, F. H. 1980, ApJ, 238, 148
Blitz, L., & Stark, A. A. 1986, ApJ, 300, L89
Blitz, L., & Thaddeus, P. 1980, ApJ, 241, 676
Block, D. L., Dyson, J. E., & Madsen, C. 1992, ApJ, 390, L13
Bloemen, J. B. G. M., et al. 1986, A&A, 154, 25
Burton, W. B., Liszt, H. S., & Baker, P. L. 1978, ApJ, 219, L67
Castelaz, M. W., et al. 1985, AJ, 90, 1113
Castets, A., Duvert, G., Dutrey, A., Bally, J., Langer, W. D., & Wilson, R. W. 1990, A&A, 234, 469
Celnik, W. E. 1983, A&AS, 53, 403
Cohen, M. 1973, ApJ, 185, L75
Cox, P., Deharveng, L., & Leene, A. 1991, A&A, 230, 171
Dame, T. M. 1993, in Back to the Galaxy, ed. S. S. Holt & F. Verter (New York: AIP), 267
Dickman, R. L. 1978, ApJS, 37, 407
Digel, S. W., Hunter, S. D., & Mukherjee, R. 1994, ApJ, 441, 270
Elmegreen, B. G., & Lada, C. J. 1977, ApJ, 214, 725
Esposito, L. W., & Colwell, J. E. 1989, Nature, 339, 605
Feldt, C. 1993, A&A, 276, 531
Field, G. B., & Saslaw, W. C. 1965, ApJ, 142, 568
Gierens, K. M., Stutzki, J., & Winnewisser, G. 1992, A&A, 259, 271
Hanson, M. M, Geballe, T. R., Conti, P. S., & Block, D. L. 1993, A&A, 273, L44
Hartmann, W. K. 1969, Icarus, 10, 201
Helfer, T. T., & Blitz, L. 1995, ApJ, 450, in press
Hollenbach, D. J., Takahashi, T., & Tielens, A. G. G. M. 1991, ApJ, 377, 192
Howe, J. E., Jaffe, D. T., Genzel, R., & Stacey, G. J. 1991, ApJ, 373, 158
Hunter, S. D., Digel, S. W., de Geus, E. J., & Kanbach, G. 1994, ApJ, 436, 216
IRAS Catalogs and Atlases: Explanatory Supplement. 1988, ed. C. A. Beichman, G. Neugebauer, H. J. Habing, P. E. Clegg, & T. J. Chester (Washington: GPO)
IRAS Point Source Catalog, Version 2. 1988, Joint *IRAS* Science Working Group (Washington: GPO) (PSC)
Kuchar, T. A., & Bania, T. M. 1993, ApJ, 414, 664
Kwan, J. 1979, ApJ, 229, 567
Lada, E. A., Bally, J., & Stark, A. A. 1991, ApJ, 368, 432
Leisawitz, D. 1990, ApJ, 359, 319
Lissauer, J. J., & Stewart, G. R. 1993, in Protostars and Planets III, ed. E. H. Levy & L. I. Lunine (Tucson: Univ. Arizona Press), 1076
Maddalena, R. & Thaddeus, P. 1985, ApJ, 294, 231
Magnani, L., Blitz, L., & Mundy, L. 1985, ApJ, 295, 402
Mathis, J. S., Rumpl, W., & Nordsieck, K. H. 1977, ApJ, 217, 425
McKee, C. F., & Williams, J. P. 1995, ApJ, submitted
Myers, P. C., Dame, T. M., Thaddeus, P., Cohen, R. S., Silverberg, R. F., Dwek, E., & Hauser, M. G. 1986, ApJ, 301, 398
Patel, N. A., Xie, T., & Goldsmith, P. F. 1993, ApJ, 413, 593
Phelps, R. L., & Lada, E. A. 1995, ApJ, submitted
Pound, M. 1994, Ph.D. thesis, Univ. Maryland
Reach, W. T., Koo, B. C., & Heiles, C. 1994, ApJ, 429, 672
Scalo, J. M. 1986, Fund. Cosmic Phys., 11, 1
Spergel, D. N., & Blitz, L. 1992, Nature, 357, 665
Stutzki, J., & Güsten, R. 1990, ApJ, 356, 513.
Stutzki, J., Stacey, G. J., Genzel, R., Harris, A. I., Jaffe, D. T., & Lugten, J. B. 1988, ApJ, 332, 379
Wannier, P. G., Andersson, B. G., Morris, M., & Lichten, S. M. 1991, ApJS, 75, 987
Williams, J. P, de Geus, E. J., & Blitz, L. 1994, ApJ, 428, 693 (WGB)
Williams, J. P, & McKee, C. F. 1995, ApJ, submitted
Wouterloot, J. G. A., Brand, J., Burton, W. B., & Kwee, K. K. 1990, A&A, 230, 21
Wouterloot, J. G. A., & Walmsley, C. M. 1986, A&A, 168, 237